

University of Leipzig
Faculty of Physics and Earth Sciences
Leipzig Institute for Meteorology - LIM

**Retrieval of aerosol optical and microphysical properties in
Cyprus during A-LIFE and CyCARE by lidar and closure
studies with airborne in-situ measurements – Towards
aerosol-cloud interaction investigations**

MASTER THESIS

Claudia Urbanneck

Primary Consultant: Prof. Dr. Andreas Macke
Secondary Consultant: Prof. Dr. Manfred Wendisch

23 October 2018

Contents

1	Introduction	1
2	Theory	5
2.1	Lidar principle	5
2.2	Klett method	6
2.3	Raman-lidar method	7
2.4	Aerosol optical properties	8
2.5	Microphysical properties	11
2.5.1	Particle type separation	11
2.5.2	Particle number and surface area concentration profiles	14
2.5.3	CCN and INP number concentration profiles	16
3	Measurement campaigns	19
3.1	CyCARE	19
3.1.1	Overview	19
3.1.2	Polly ^{XT}	19
3.2	A-LIFE	21
4	Case studies	25
4.1	06 April 2017	25
4.2	21 April 2017	36
4.3	26/27 April 2017	46
5	Comparison with A-LIFE measurements	57
6	Conclusion and Outlook	61
	List of Figures	65
	List of Tables	69
	Bibliography	71

1 Introduction

Aerosol particles have diverse impacts on human life. While they affect, e.g. air quality and aviation safety, their most important role lies in their effects on the Earth's energy budget. Acting as scatterers and absorbers of solar radiation in the atmosphere, aerosol particles directly influence the distribution of energy. Additionally, an indirect radiative forcing can be attributed to them with regard to their interaction with clouds since they can act as cloud condensation nuclei (CCN) or ice nucleating particles (INP) to induce cloud formation.

In the case of liquid water, the Twomey effect describes the impact of particles on cloud droplet number concentration and size: an abundance of CCN encourages the formation of many small droplets. These have a larger reflecting surface than fewer bigger droplets. Therefore, aerosol particles affect the albedo of clouds (Twomey, 2007). Furthermore, smaller droplets have a lower probability of raining out, thus increasing the lifetime of clouds (Albrecht, 1989).

Below 0°C , ice formation can take place in different ways. Pure water automatically crystallises only below -36°C due to its thermodynamic properties at that temperature. This process is called homogeneous freezing. Between 0 and -36°C , freezing can be triggered by ice nuclei, e.g. particles such as mineral dust or black carbon. Even bacteria may induce this so-called heterogeneous freezing (Emersic, 2018). Depending on the way of interaction of ice nucleus and supercooled water, heterogeneous freezing may be further distinguished into deposition nucleation, immersion freezing, condensation freezing and contact freezing. Specifically immersion freezing, i.e. a particle suspended in a supercooled water droplet and inducing the freezing process, is of key importance for the formation of ice in mixed-phase clouds (Tobo, 2016).

All in all, the largest uncertainty for weather and future-climate predictions is still posed by the effects of cloud-aerosol interaction on Earth's energy budget (IPCC, 2013).

Apart from their interaction with clouds, aerosol particles themselves are complex with regard to their size, shape, chemical composition and spatially and temporally variable distribution in the atmosphere (Baars et al., 2016).

Thus, continuous observation and typing of aerosol conditions is necessary to provide a foundation for a better understanding of their influence on Earth's climate and the provision of CCN.

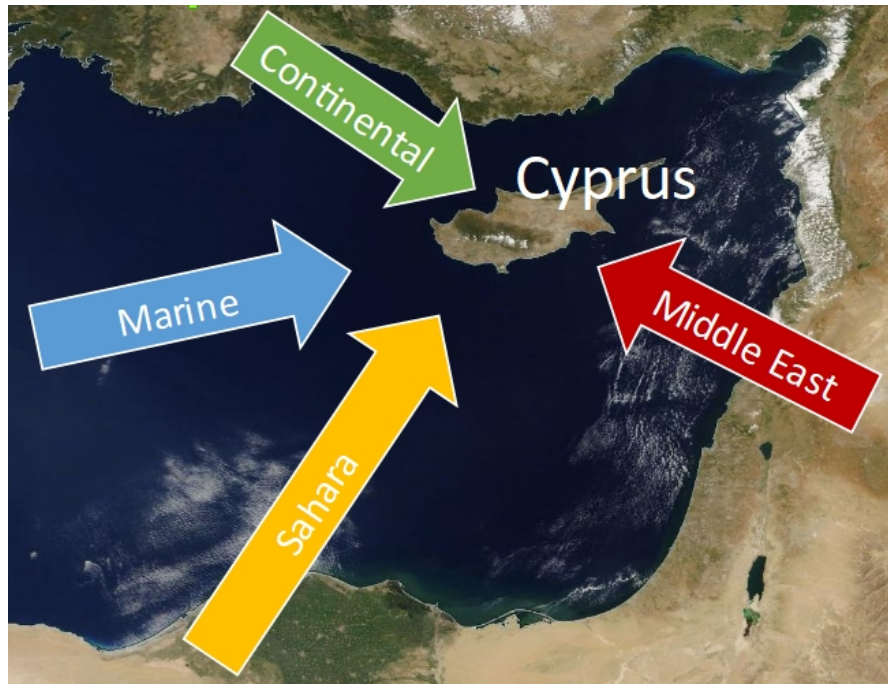


Figure 1.1: Sketch indicating the aerosol transport to Cyprus in the Eastern Mediterranean. (Picture provided by TROPOS)

The active remote sensing instrument lidar can be used to obtain vertical structures of aerosols and to type particles according to their optical properties. Its measurements typically show regional aerosol influences in the lowermost troposphere as well as long-range transported particles in the free atmosphere. Hence, lidar is an appropriate tool for aerosol observations and research.

An identified hot spot regarding climate change and aerosol load is Cyprus. As an island in the Eastern Mediterranean, Cyprus is defined by an intense Mediterranean climate with a typical seasonal rhythm of hot and dry summers, lasting from mid-May to mid-September, and rainy winters from November to March (Department of Meteorology, Republic of Cyprus, 2018).

It is affected by several different types of aerosols, making it one of the most polluted areas of the world (Weinzierl, 2014). Mineral dust originating from the Sahara or Middle-Eastern deserts, marine aerosol, aged anthropogenic particles as well as smoke from the North can all be regularly found in the atmosphere above Cyprus. Fig. 1.1 shows the directions of transport of these different aerosols to Cyprus. Therefore, it provides an interesting natural laboratory for aerosol studies and has attracted field campaigns of

multiple initiatives like INUIT (Ice Nuclei Research Unit), BACCHUS (Impact of Biogenic versus Anthropogenic emissions on Clouds and Climate: towards a Holistic Understanding), ACTRIS (Aerosols, Clouds and Trace gases Research InfraStructure), and most recently A-LIFE (Absorbing aerosol layers in a changing climate: aging, LIFETIME and dynamics) and CyCARE (Cyprus Clouds Aerosol and Rain Experiment), which are the focus of this thesis.

In this work, lidar measurements performed during the CyCARE field campaign are analysed in order to type the aerosol particles on days with heavy aerosol load. Based on this analysis, particle number and surface area concentrations as well as CCN and INP number concentrations are estimated following the concept of Mamouri and Ansmann (2016) to make full use of the data sets provided by the deployed Raman polarisation lidar. Differing from Mamouri and Ansmann (2016), a more recent INP parameterisation found by Ullrich et al. (2017) is applied.

Furthermore, the results of this analysis are to be used as basis for extensive comparisons with A-LIFE's in-situ measurements. Within the framework of this thesis, a first comparison of lidar-derived particle number concentration and preliminary results of the in-situ measurements is performed in order to test and validate the applicability of the data analysis scheme provided by Mamouri and Ansmann (2016). The potential of lidar to provide aerosol parameters, which are relevant for the formation of clouds, meaning both liquid-water droplet and ice crystal nucleation, is further explored. Thus, the importance of this remote sensing instrument in the field of aerosol and cloud research increases due to its potential to provide reliable results without the need for in-situ measurement efforts.

The structure of this work is as follows: Chapter 2 provides background information on lidar techniques, the retrieval of aerosol optical properties and, based on that, the derivation of microphysical properties. Descriptions of the two campaigns CyCARE and A-LIFE, which provided the data analysed in the framework of this thesis, are given in chapter 3. From these campaigns, three dates of interest in April 2017 were chosen for a full lidar-based analysis. This analysis as well as a comparison to preliminary results from A-LIFE's in-situ measurements are shown and discussed in chapters 4 and 5, respectively. Chapter 6 concludes this work with a summary of the most important results.

2 Theory

2.1 Lidar principle

LIDAR (Light Detection and Ranging) is a method in the active remote sensing field, which can be used to investigate the vertical structure of the atmosphere with regard to aerosols. Monochromatic and coherent laser pulses are being emitted and can be absorbed or scattered by molecules and atmospheric particles. A telescope detects the backscattered light. The scattering height level or “range” R from the lidar can be calculated using the time t between pulse emission and signal detection and the speed of light c :

$$R = \frac{ct}{2} \quad (2.1)$$

The factor $\frac{1}{2}$ in Eq. 2.1 accounts for the twofold covered atmospheric way of the emitted pulse to the backscattering air mass and back to the instrument.

The detected signal P at wavelength λ in the scattering height is described by the lidar equation for elastic scattering according to Wandinger (2005) as:

$$P(R, \lambda) = \underbrace{P_0(\lambda) \frac{c\tau(\lambda)}{2} \eta(\lambda) A_{\text{Tel}}}_{1} \cdot \underbrace{\frac{O(R)}{R^2}}_{2} \cdot \underbrace{[\beta_{\text{mol}}(R, \lambda) + \beta_{\text{par}}(R, \lambda)]}_{3} \cdot \underbrace{\exp[-2 \int_0^R \alpha(r, \lambda) dr]}_{4} \quad (2.2)$$

Term 1 on the right-hand side of the equation shows the system factor, which contains the (height independent) instrument specific parameters. These are the power of the emitted laser pulse P_0 , the temporal pulse length $\tau(\lambda)$, the transmission efficiency $\eta(\lambda)$ and the area of the receiver telescope A_{Tel} .

The second term indicates the range-dependent geometrical measurement properties. It includes the overlap function $O(R)$ of laser beam and the receiver’s field of view, as well as the squared decrease in signal power with distance between instrument and scattering volume. Close to the lidar $O(R)$ is 0 while in regions with full overlap $O(R)$ has its maximum value of 1.

The backscatter coefficient $\beta(R, \lambda)$, which forms term 3, determines the amount of photons scattered at 180° directly back at the receiver. Backscattering can be caused by molecules (index mol) or particles (index par).

The fourth term of the equation is the transmission term. This last term describes the attenuation of radiation through scattering and absorption by both molecules and particles. The extinction coefficient can therefore also be written as:

$$\alpha(r, \lambda) = \alpha_{\text{mol,sca}}(r, \lambda) + \alpha_{\text{mol,abs}}(r, \lambda) + \alpha_{\text{par,sca}}(r, \lambda) + \alpha_{\text{par,abs}}(r, \lambda) \quad (2.3)$$

It is being integrated over the range from lidar ($R = 0$) to height R . The factor 2 again accounts for the two-way photon travel.

Since the intensity of the received signal decreases with distance, it can be converted to the range-corrected signal by multiplication with R^2 :

$$P(R, \lambda)R^2 = P_0(\lambda) \frac{c\tau(\lambda)}{2} \eta(\lambda) A_{\text{Tel}} \cdot O(R) \cdot [\beta_{\text{mol}}(R, \lambda) + \beta_{\text{par}}(R, \lambda)] \cdot \exp\left\{-2 \int_0^R [\alpha_{\text{mol}}(r, \lambda) + \alpha_{\text{par}}(r, \lambda)] dr\right\} \quad (2.4)$$

Both backscatter and extinction coefficients are used as basis for the characterisation of the scattering particles. Two methods to derive those coefficients are the Klett method and the Raman-lidar method.

2.2 Klett method

The particle backscatter coefficient can be calculated by use of the following equation (Klett, 1981):

$$\beta_{\text{par}}(R, \lambda_0) = \frac{A(R, R_0, \lambda_0)}{B(R_0, \lambda_0) - 2S_{\text{par}}(\lambda_0) \int_{R_0}^R A(R_0, r, \lambda_0) dr} - \beta_{\text{mol}}(R, \lambda_0) \quad (2.5)$$

with

$$A(x, R_0, \lambda_0) = x^2 P(x, \lambda_0) \cdot \exp\left\{-2[S_{\text{par}}(\lambda_0) - S_{\text{mol}}] \int_{R_0}^x \beta_{\text{mol}}(r, \lambda_0) dr\right\} \quad (2.6)$$

and

$$B(R_0, \lambda_0) = \frac{R_0^2 P(R_0, \lambda_0)}{\beta_{\text{par}}(R_0, \lambda_0) + \beta_{\text{mol}}(R_0, \lambda_0)} \quad (2.7)$$

A reference height R_0 is introduced, where the particle backscatter coefficient $\beta_{\text{par}}(R_0, \lambda_0)$ is assumed to be very small compared to the known Rayleigh scattering. To solve Eq. 2.5, the particle lidar ratio

$$S_{\text{par}}(R, \lambda_0) = \frac{\alpha_{\text{par}}(R, \lambda_0)}{\beta_{\text{par}}(R, \lambda_0)} \quad (2.8)$$

has to be assumed as well. Depending on the expected atmospheric situation at hand, a characteristic value for the type of aerosol is chosen. By this method though, the retrieved α_{par} is strongly dependent on this assumption. The molecule-related lidar ratio S_{mol} is analogically defined by the ratio of molecular extinction to backscatter coefficients (Eq. 2.12).

2.3 Raman-lidar method

For the independent determination of backscatter and extinction coefficients, the Raman-lidar method may be applied. Additionally to the elastically backscattered signal, the inelastically backscattered signal $P(R, \lambda_{\text{Ra}})$ needs to be measured for this method. During inelastic scattering, part of the photon's energy is transferred to the molecules, which translates to a shift in wavelength. The resulting wavelength is called Raman wavelength λ_{Ra} . The detected power at this wavelength is described analogically to Eq. 2.2 by Wandinger (2005):

$$P(R, \lambda_{\text{Ra}}) = \underbrace{P_0(\lambda_0) \frac{c\tau(\lambda_{\text{Ra}})}{2} \eta(\lambda_{\text{Ra}}) A_{\text{Tel}}}_{1} \cdot \underbrace{\frac{O(R)}{R^2}}_{2} \cdot \underbrace{\beta_{\text{Ra}}(R, \lambda_{\text{Ra}})}_{3} \cdot \underbrace{\exp\left[-\int_0^R \alpha(r, \lambda_0) + \alpha(r, \lambda_{\text{Ra}}) dr\right]}_{4} \quad (2.9)$$

The system factor 1 now contains a λ_{Ra} dependent temporal pulse length $\tau(\lambda_{\text{Ra}})$ and system efficiency $\eta(\lambda_{\text{Ra}})$. The geometry factor (term 2) ideally remains unchanged but the backscatter coefficient in term 3 is measured at the Raman wavelength. The transmission term now consists of an elastic part for the way up ($\alpha(\lambda_0)$) and an inelastic part for the way back ($\alpha(\lambda_{\text{Ra}})$) to the receiver. Using a Raman-lidar, the backscatter coefficient is calculated as (Ansmann et al., 1992):

$$\beta_{\text{par}}(R, \lambda_0) = [\beta_{\text{par}}(R_0, \lambda_0) + \beta_{\text{mol}}(R_0, \lambda_0)] \cdot \frac{P(R_0, \lambda_{\text{Ra}})P(R, \lambda_0)N_{\text{Ra}}(R)}{P(R_0, \lambda_0)P(R, \lambda_{\text{Ra}})N_{\text{Ra}}(R_0)} \cdot \frac{\exp\left\{-\int_{R_0}^R [\alpha_{\text{mol}}(r, \lambda_{\text{Ra}}) + \alpha_{\text{par}}(r, \lambda_{\text{Ra}})] dr\right\}}{\exp\left\{-\int_{R_0}^R [\alpha_{\text{mol}}(r, \lambda_0) + \alpha_{\text{par}}(r, \lambda_0)] dr\right\}} - \beta_{\text{mol}}(R, \lambda_0) \quad (2.10)$$

Like in Eq. 2.5, R_0 is a reference height, in which the pure molecular signal dominates and $\beta(R_0, \lambda_0)$ is assumed a priori. N_{Ra} indicates the molecular particle number density of the regarded gas. The particle number density profiles of oxygen and nitrogen are sufficiently well known and can be easily calculated by temperature and pressure profiles derived from radio soundings or atmospheric model data. In this work, GDAS1 data was utilised for this calculation.

The extinction coefficient is determined as (Ansmann et al., 1990):

$$\alpha_{\text{par}}(R, \lambda_0) = \frac{\frac{d}{dR} \left[\ln \frac{N_{\text{Ra}}(R)}{R^2 P_{\text{Ra}}(R)} \right] - \alpha_{\text{mol}}(R, \lambda_0) - \alpha_{\text{mol}}(R, \lambda_{\text{Ra}})}{1 + \left(\frac{\lambda_0}{\lambda_{\text{Ra}}} \right)^{\hat{a}_\alpha}} \quad (2.11)$$

Here, \mathring{a}_α describes the Ångström exponent, a quantity that reflects the wavelength dependency of the extinction coefficient.

Since they are extensive parameters, neither backscatter nor extinction coefficients are suitable to type aerosol particles. Instead, they can be used to derive intensive parameters, namely lidar ratio, Ångström exponent and depolarisation ratio, which are useful for aerosol classification.

2.4 Aerosol optical properties

The lidar ratio

$$S_{\text{mol}}(R, \lambda) = \frac{\alpha_{\text{mol}}(R, \lambda)}{\beta_{\text{mol}}(R, \lambda)} \quad (2.12)$$

$$S_{\text{par}}(R, \lambda) = \frac{\alpha_{\text{par}}(R, \lambda)}{\beta_{\text{par}}(R, \lambda)} \quad (2.13)$$

expresses the relationship between backscatter and extinction coefficient for molecules and particles and can be used as a measure for absorption. As it is dependent on the size distribution, size and chemical composition of the scattering particles, it is a key factor for determining the type of aerosol.

The Ångström exponent can be derived from backscatter or extinction coefficients, measured at two different wavelengths λ_0 and λ_1 as:

$$\mathring{a}_\beta = -\frac{\ln\left(\frac{\beta_{\text{par}}(\lambda_1)}{\beta_{\text{par}}(\lambda_0)}\right)}{\ln\left(\frac{\lambda_1}{\lambda_0}\right)} \quad (2.14)$$

$$\mathring{a}_\alpha = -\frac{\ln\left(\frac{\alpha_{\text{par}}(\lambda_1)}{\alpha_{\text{par}}(\lambda_0)}\right)}{\ln\left(\frac{\lambda_1}{\lambda_0}\right)} \quad (2.15)$$

It is inversely proportional to the particle size, yielding larger values for smaller particles and values close to zero for large particles such as mineral dust.

During the scattering process, the state of polarisation of the emitted light can change due to the particle geometrical properties. While the emitted laser light is linear polarised, the detected signal contains a cross-polarised component P_\perp as well as a linear polarised one P_\parallel . The two components are given as:

$$P_\perp(R, \lambda) = P_0(\lambda) \frac{c\tau(\lambda)}{2} \eta_\perp(\lambda) A_{\text{Tel}} \cdot \frac{O(R)}{R^2} \cdot \beta_\perp(R, \lambda) \cdot \exp\left[-2 \int_0^R \alpha(r, \lambda) dr\right] \quad (2.16)$$

$$P_\parallel(R, \lambda) = P_0(\lambda) \frac{c\tau(\lambda)}{2} \eta_\parallel(\lambda) A_{\text{Tel}} \cdot \frac{O(R)}{R^2} \cdot \beta_\parallel(R, \lambda) \cdot \exp\left[-2 \int_0^R \alpha(r, \lambda) dr\right] \quad (2.17)$$

The volume depolarisation ratio δ_{vol} is therefore determined by the cross-polarised and the parallel-polarised backscatter coefficients β_{\perp} and β_{\parallel} , which both can be separated into molecular and particle backscatter coefficients:

$$\delta_{\text{vol}}(R, \lambda) = C \frac{P_{\perp}(R, \lambda)}{P_{\parallel}(R, \lambda)} = C \frac{\beta_{\perp}(R, \lambda)}{\beta_{\parallel}(R, \lambda)} = C \frac{\beta_{\text{mol},\perp}(R, \lambda) + \beta_{\text{par},\perp}(R, \lambda)}{\beta_{\text{mol},\parallel}(R, \lambda) + \beta_{\text{par},\parallel}(R, \lambda)} \quad (2.18)$$

Since the system efficiencies of the cross-polarised and the parallel-polarised signal are different, it is necessary to introduce a calibration constant C . In this work, the $\pm 45^{\circ}$ calibration method according to Freudenthaler et al. (2009) was applied.

Analogically to the volume depolarisation ratio, the molecular and particle depolarisation ratios are:

$$\delta_{\text{mol}}(R, \lambda) = \frac{\beta_{\text{mol},\perp}(R, \lambda)}{\beta_{\text{mol},\parallel}(R, \lambda)} \quad (2.19)$$

$$\delta_{\text{par}}(R, \lambda) = \frac{\beta_{\text{par},\perp}(R, \lambda)}{\beta_{\text{par},\parallel}(R, \lambda)} \quad (2.20)$$

After the separation of molecular and particle contributions, the particle depolarisation ratio can be expressed according to Tesche et al. (2009a) as:

$$\delta_{\text{par}}(R, \lambda) = \frac{\beta_{\text{mol}}(R, \lambda)(\delta_{\text{vol}}(R, \lambda) - \delta_{\text{mol}}(R, \lambda)) + \beta_{\text{par}}(R, \lambda)\delta_{\text{vol}}(R, \lambda)(1 + \delta_{\text{mol}}(R, \lambda))}{\beta_{\text{mol}}(R, \lambda)(\delta_{\text{mol}}(R, \lambda) - \delta_{\text{vol}}(R, \lambda)) + \beta_{\text{par}}(R, \lambda)(1 + \delta_{\text{mol}}(R, \lambda))} \quad (2.21)$$

The state of polarisation of the backscattered light holds information about the sphericity of the scattering particles. Spherical particles, e.g. water droplets, do not produce any depolarisation during the backscatter process. Therefore, their depolarisation ratio is close to zero. Backscattering by non-spherical particles such as ice crystals and mineral dust yields a considerably higher depolarisation ratio.

An overview of characteristic lidar and depolarisation ratios at 355 nm for different aerosol types is shown in Fig. 2.1. These values were derived from ground-based measurements performed by Raman-polarisation lidars at Cape Verde (Groß et al., 2011), Leipzig, Munich (Groß et al., 2012), the Amazon Basin (Baars et al., 2012) and over the North Atlantic (Kanitz et al., 2013).

The largest differences between the various particle types are found in the depolarisation ratio. It varies between 2 to 6 % for smoke, pollution and marine aerosols and up to 40 % for volcanic ash. Dust and dust mixtures usually produce a depolarisation ratio of 15 to 31 %.

Lidar ratios are lowest for marine aerosol, usually yielding 10-30 sr, and highest for smoke and dust-smoke mixtures with up to 95 sr. Other aerosol types are in the range of 40 to 60 sr.

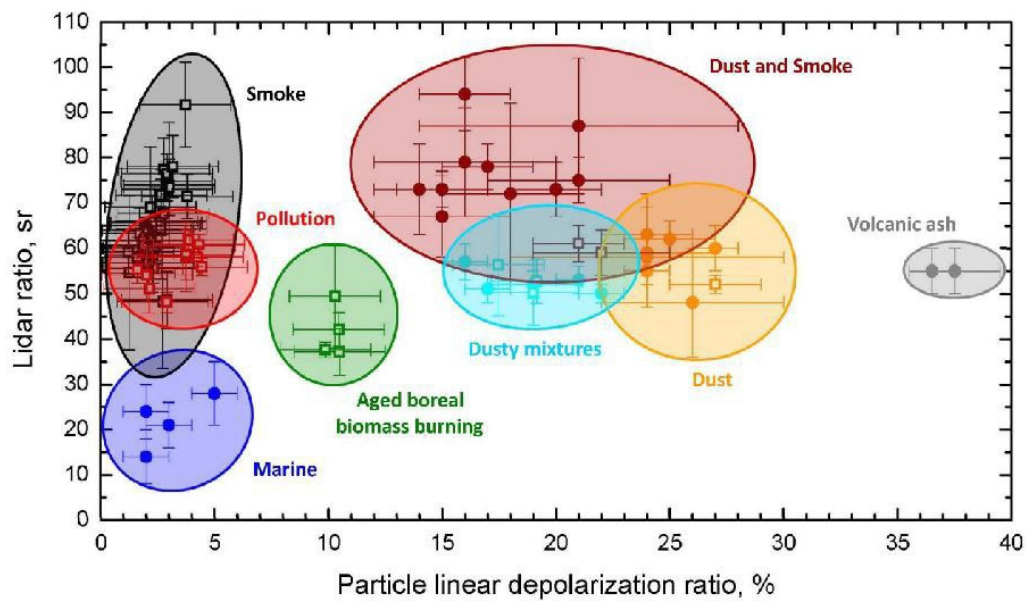


Figure 2.1: Classification of different aerosol types by lidar and depolarisation ratio at 355 nm. The used data includes measurements by TROPOS (dots) and the University of Munich (open squares) at Cape Verde, Leipzig, Munich, the Amazon Basin and over the North Atlantic (Illingworth et al., 2015).

2.5 Microphysical properties

The potency of aerosol particles to act as CCN or INP and therefore the reservoir of cloud-relevant particles (n_{CCN}) and the number concentration of INP (n_{INP}) strongly depend on the aerosol particle type. For cloud droplet formation, according to Mamouri and Ansmann (2016), a distinction between non-desert and desert dust particles is necessary since the former, consisting of continental (mixtures of anthropogenic haze, biomass burning smoke, soil and road dust, and organic and biogenic particles from soils and plants) and marine aerosol components with dry radius > 50 nm, get activated at low supersaturations of 0.1 - 0.2 %, i.e. a relative humidity of 100.1 - 100.2 %, while the critical activation radius of hydrophobic insoluble desert dust particles with a negligible soluble coating is > 100 nm (Koehler et al., 2009; Kumar et al., 2011).

The case of INP is even more complex as the type of favorable particle for heterogeneous ice formation is also dependent on the temperature regime. At temperatures below -20 °C, mineral dust acts as efficient INP, whereas marine particles seem comparably inefficient. In contrast, continental aerosols always contain efficient INP that allow for ice nucleation at higher temperatures (-5 to -15 °C) (Mamouri and Ansmann, 2016).

A relatively simple approach to estimate n_{CCN} and n_{INP} , that doesn't require comprehensive data analysis methods and a good knowledge in the use of illposed inversion techniques but allows fast computation and implementation of an automated code, is presented by Mamouri and Ansmann (2016).

Fig. 2.2 gives an overview of their data analysis scheme as it was applied for this work. In the following subsections, each of the steps will be explained in detail. It should be noted that only the 532 nm backscatter coefficient was used for calculations since it yields the most robust results (Mamouri and Ansmann, 2017).

2.5.1 Particle type separation

In order to allow an estimate of the contribution of each aerosol type, firstly, the polarisation-lidar photometer networking method (POLIPHON, Ansmann et al. (2011, 2012)) is applied to separate the retrieved backscatter coefficient profiles into dust and non-dust portions as outlined below.

Both the parallel-polarised backscatter coefficient $\beta_{\text{par},\parallel}$ and the cross-polarised backscatter coefficient $\beta_{\text{par},\perp}$ are assumed to be composed of dust (index d) and non-dust (index nd) components:

$$\beta_{\text{par},\parallel} = \beta_{\parallel,\text{d}} + \beta_{\parallel,\text{nd}} \quad (2.22)$$

$$\beta_{\text{par},\perp} = \beta_{\perp,\text{d}} + \beta_{\perp,\text{nd}} \quad (2.23)$$

Thus, the particle depolarisation ratio (Eq.2.20) may be expressed as

$$\delta_{\text{par}} = \frac{\beta_{\perp,\text{d}} + \beta_{\perp,\text{nd}}}{\beta_{\parallel,\text{d}} + \beta_{\parallel,\text{nd}}} \quad (2.24)$$

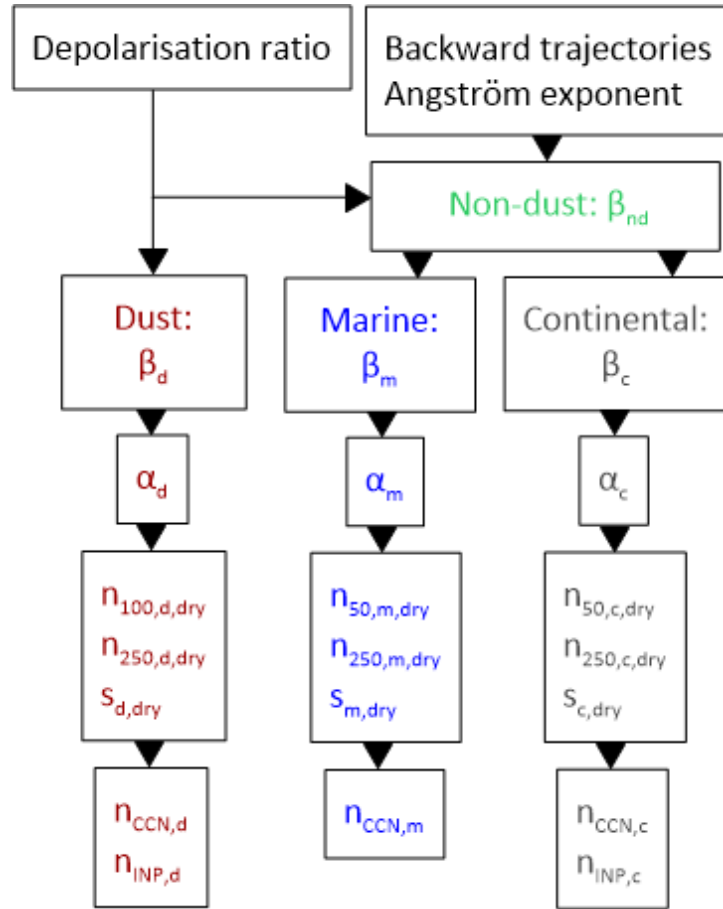


Figure 2.2: Overview of the data analysis scheme used to derive the microphysical particle properties, and the estimated cloud-relevant quantities from aerosol optical properties. The use of a polarisation lidar allows for the separation of dust and non-dust backscatter coefficients β_d and β_{nd} via the particle depolarisation ratio. The distinction of the non-dust contribution into marine (β_m) and continental aerosol backscatter coefficients (β_c) may then be made utilising backward trajectory analysis and Ångström exponent information. The three backscatter coefficients are converted to respective extinction coefficients α_i , which are then converted to particle number concentrations $n_{100,d,dry}$, $n_{50,m,dry}$, $n_{50,c,dry}$ and $n_{250,i,dry}$, and surface area concentrations $s_{i,dry}$. Indices indicate the minimum dry radius in nanometers and aerosol type. In the last step, estimates of CCN number concentrations $n_{CCN,i}$ are calculated from $n_{100,d,dry}$, $n_{50,m,dry}$, $n_{50,c,dry}$, while estimates of INP number concentrations $n_{INP,i}$ are derived from $s_{i,dry}$. Adapted from Mamouri and Ansmann (2016).

Using the relations

$$\beta_d = \beta_{\parallel,d} + \beta_{\perp,d} \quad (2.25)$$

$$\beta_{nd} = \beta_{\parallel,nd} + \beta_{\perp,nd} \quad (2.26)$$

allows, according to Tesche et al. (2009a), the transformation to

$$\delta_{par} = \frac{\beta_{nd}\delta_{nd}(1 + \delta_d) + \beta_d\delta_d(1 + \delta_{nd})}{\beta_{nd}(1 + \delta_d) + \beta_d(1 + \delta_{nd})} \quad (2.27)$$

Substituting β_{nd} by $\beta_{par} - \beta_d$ and solving for β_d gives the dust backscatter coefficient

$$\beta_d = \beta_{par} \frac{(\delta_{par} - \delta_{nd})(1 + \delta_d)}{(\delta_d - \delta_{nd})(1 + \delta_{par})} \quad (2.28)$$

which is valid for particle depolarisation ratios of $\delta_{nd} \leq \delta_{par} \leq \delta_d$.

The non-dust backscatter coefficient profile is then obtained via

$$\beta_{nd} = \beta_{par} - \beta_d \quad (2.29)$$

For $\delta_{par} \leq \delta_{nd}$, this method yields $\beta_{nd} = \beta_{par}$, and $\beta_d = \beta_{par}$ for $\delta_{par} \geq \delta_d$.

The fraction of dust particles is assumed to contain only coarse mode dust particles with this approach (Mamouri and Ansmann, 2014).

After the distinction between dust and non-dust backscatter coefficients by use of the depolarisation ratio, backward trajectories and Ångström exponent help to further separate the non-dust contribution into continental and marine backscatter coefficients. Based on this, in the presented cases, a small marine contribution of 20 % is assumed in the planetary boundary layer, while in the free troposphere the non-dust contribution is attributed solely to continental type aerosol.

The obtained three backscatter coefficients β_i ($i = d$ for desert, m for marine and c for continental) are converted to extinction coefficients α_i , via multiplication with appropriate lidar ratios S_i for each of the aerosol types (see Tab. 2.1).

To assure the choice of reasonable lidar ratios, a comparison of the extinction coefficient profile measured by lidar via the Raman method $\alpha_{par,meas}$ and the from backscatter coefficients converted profile $\alpha_{par,calc}$ is necessary. Since the lidar derived extinction coefficient profile $\alpha_{par,meas}$ contains contributions of all aerosol types, it can be described by

$$\alpha_{par,meas} = \alpha_d + \alpha_c + \alpha_m \quad (2.30)$$

The afore described method analogically yields

$$\alpha_{par,calc} = S_d\beta_d + f_m S_{nd}\beta_m + f_c S_{nd}\beta_c \quad (2.31)$$

Here, f_i describes the relative contribution of the non-dust aerosol types (Mamouri and Ansmann, 2017).

Parameter	Value	Reference
δ_d	0.31	Mamouri and Ansmann (2017)
δ_{nd}	0.05	
S_d	35 - 40 sr (Middle Eastern dust) 45 - 50 sr (Saharan dust)	Mamouri and Ansmann (2016)
S_{nd}	30 - 50 sr	
S_m	20 sr	
S_c	35 - 70 sr	
ρ_d	2.6 g cm^{-3}	
ρ_{nd}	1.6 g cm^{-3}	Ansmann et al. (2012)
ν_d/τ_d	$0.61 \times 10^{-6} \text{ m}$	Mamouri and Ansmann (2017)
ν_{nd}/τ_{nd}	$0.41 \times 10^{-6} \text{ m}$	

Table 2.1: Applied values for each of the parameters required for the determination of dust and non-dust contributions and the subsequent calculation of extinction coefficient and mass concentration profiles. Depolarisation ratios δ_i , particle densities ρ_i and conversion factors ν_i/τ_i are taken from literature. Lidar ratios S_i at 532 nm were varied within the range of literature values in order to find the best match between the calculated and measured extinction coefficients for each case discussed in chapter 4.

A good agreement of $\alpha_{\text{par,meas}}$ and $\alpha_{\text{par,calc}}$ is proof for reasonably chosen lidar ratios.

Additionally to extinction coefficient profiles, the derived dust and non-dust backscatter profiles make the calculation of respective mass concentration profiles possible, as shown by Ansmann et al. (2012):

$$M_d = \rho_d(\nu_d/\tau_d)S_d\beta_d \quad (2.32)$$

$$M_{nd} = \rho_{nd}(\nu_{nd}/\tau_{nd})S_{nd}\beta_{nd} \quad (2.33)$$

In these equations, ρ_i denote the particle densities, and ν_i/τ_i are conversion factors, obtained through AERONET photometer observations. The conversion factors consist of the column particle volume concentration ν_i and the optical thickness τ_i . Again, appropriate lidar ratios S_i are applied for the different aerosol types. Tab. 2.1 summarises the values used for each of the parameters mentioned in this subsection.

2.5.2 Particle number and surface area concentration profiles

The retrieved particle extinction coefficients may be converted to profiles of particle number concentrations $n_{100,d,dry}$, $n_{250,d,dry}$, $n_{50,m,dry}$, $n_{250,m,dry}$, $n_{50,c,dry}$ and $n_{250,c,dry}$, and surface area concentrations $s_{d,dry}$, $s_{m,dry}$ and $s_{c,dry}$. The indices indicate the dry minimum radius in nanometers and aerosol type.

In the case of hydrophobic dust particles, no correction for water-uptake is necessary while for non-dust particles hygroscopic growth needs to be accounted for. According to Mamouri and Ansmann (2016) $n_{100,m}$, $n_{500,m}$ and $s_m/4$ may serve as proxies for $n_{50,m,dry}$, $n_{250,m,dry}$ and $s_{m,dry}$, and $n_{60,c}$, $n_{290,c}$ and $s_c/1.33$ for $n_{50,c,dry}$, $n_{250,c,dry}$ and $s_{c,dry}$, respectively. The correlation of $\log n_{100,d}$ with $\log \alpha_d$, $n_{250,d,dry}$ with α_d , $\log n_{100,m}$ with $\log \alpha_m$, $n_{250,m,dry}$ with α_m , $\log n_{60,c}$ with $\log \alpha_c$, and $n_{250,c,dry}$ with α_c is assumed to be a linear one.

The various particle number concentration profiles in the dry state are thus calculated using the following equations (Mamouri and Ansmann, 2016):

$$n_{100,d,dry} = c_{100,d} \cdot \alpha_d^{\chi_d} \quad (2.34)$$

$$n_{250,d,dry} = c_{250,d} \cdot \alpha_d \quad (2.35)$$

$$n_{50,m,dry} = c_{100,m} \cdot \alpha_m^{\chi_m} \quad (2.36)$$

$$n_{250,m,dry} = c_{500,m} \cdot \alpha_m \quad (2.37)$$

$$n_{50,c,dry} = c_{60,c} \cdot \alpha_c^{\chi_c} \quad (2.38)$$

$$n_{250,c,dry} = c_{290,c} \cdot \alpha_c \quad (2.39)$$

with particle extinction coefficients in Mm^{-1} and particle number concentrations in cm^{-3} . The conversion parameters c_i (in Mm cm^{-3}) and extinction exponents χ_i have been obtained from a correlation study, performed by Mamouri and Ansmann (2016), using long-term AERONET and field campaign data. While parameters for Limassol, Cyprus, are available from this study, for the cases presented in chapter 4, the conversion parameters for Leipzig, Germany, and Barbados have been found to be a better fit for continental aerosol and dust, respectively (Albert Ansmann, personal communication, July 2018).

Furthermore, the particle surface area concentrations $s_{i,dry}$ are derived in $\text{m}^2 \text{cm}^{-3}$ by linear correlations with the particle extinction coefficients:

$$s_{d,dry} = c_{s,d} \cdot \alpha_d \quad (2.40)$$

$$s_{m,dry} = c_{s,m}/4 \cdot \alpha_m \quad (2.41)$$

$$s_{c,dry} = c_{s,c}/1.33 \cdot \alpha_c \quad (2.42)$$

with the conversion factors $c_{s,i}$ in $\text{Mm m}^2 \text{cm}^{-3}$ (Mamouri and Ansmann, 2016). All used parameters, their values and their units are summarised in Tab. 2.2.

Parameter	Value	Unit
$c_{100,d}$	6.50	Mm cm ⁻³
χ_d	0.70	
$c_{250,d}$	0.20	Mm cm ⁻³
$c_{s,d}$	1.94×10^{-12}	Mm m ² cm ⁻³
$c_{100,m}$	7.20	Mm cm ⁻³
χ_m	0.85	
$c_{500,m}$	0.06	Mm cm ⁻³
$c_{s,m}/4$	0.63×10^{-12}	Mm m ² cm ⁻³
$c_{60,c}$	25.3	Mm cm ⁻³
χ_c	0.94	
$c_{290,c}$	0.10	Mm cm ⁻³
$c_{s,c}/1.33$	2.80×10^{-12}	Mm m ² cm ⁻³

Table 2.2: Conversion parameters used for the calculation of particle number and surface area concentration profiles. Adapted from Mamouri and Ansmann (2016).

2.5.3 CCN and INP number concentration profiles

To estimate CCN-relevant particle number concentrations $n_{CCN,i}$, only a basic approach is used. In general, the size and chemical composition of a given particle, as well as the level of ambient supersaturation determine its ability to act as CCN. The number concentrations of CCN provided by the various aerosol types can be calculated as (Mamouri and Ansmann, 2016):

$$n_{CCN,ss,d} = f_{ss,d} \cdot n_{100,d,dry} \quad (2.43)$$

$$n_{CCN,ss,m} = f_{ss,m} \cdot n_{50,m,dry} \quad (2.44)$$

$$n_{CCN,ss,c} = f_{ss,c} \cdot n_{50,c,dry} \quad (2.45)$$

where $f_{ss,i}$ is an enhancement factor, depending on the supersaturation of the surrounding cloud layer. For very low supersaturations of 0.1-0.2%, this factor is assumed to be $f_{ss=0.15\%,i} = 1.0$, i.e. the respective number concentrations also represent the number concentrations of CCN. A higher supersaturation allows for smaller particles to be activated, thus increasing the $n_{CCN,i}$. To account for this effect Mamouri and Ansmann (2016) estimated $f_{ss=0.25\%,i} = 1.35$, and $f_{ss=0.4\%,i} = 1.7$ for higher supersaturations. In this work, a moderate supersaturation of 0.25% was assumed for $n_{CCN,i}$ calculations.

The number concentrations of INP can be derived from the surface area concentrations via the relation

$$n_{INP,d}(T) = 1000 \cdot s_{d,dry} \cdot \eta_{k,d}(T) \quad (2.46)$$

in the case of desert dust, and for soot via

$$n_{INP,s}(T) = 1000 \cdot s_{c,dry} \cdot \eta_{k,s}(T) \quad (2.47)$$

The factor 1000 is included to derive $n_{\text{INP},i}$ in L^{-1} . $\eta_{k,i}(T)$ is a parameterisation term including the temperature dependency of $n_{\text{INP},i}$ for immersion freezing ($k = \text{im}$) and deposition freezing ($k = \text{dep}$), respectively (Mamouri and Ansmann, 2016). Ullrich et al. (2017) conducted heterogeneous freezing experiments at the Aerosol Interaction and Dynamics in the Atmosphere (AIDA) chamber in Karlsruhe, Germany, finding the following empirical parameterisation terms for desert dust and soot:

$$\eta_{\text{im,d}}(T) = \exp(150.577 - 0.517 \cdot T) \quad (2.48)$$

for $T \in [243, 259]$ K,

$$\eta_{\text{dep,d}}(T) = \exp\{285.692(ss_{\text{ice}} - 1)^{\frac{1}{4}} \cdot \cos[0.017(T - 256.692)]^2 \cdot \text{arccot}[0.080(T - 200.745)]/\pi\} \quad (2.49)$$

for $T \in [206, 235]$ K,

$$\eta_{\text{im,s}}(T) = 7.463 \cdot \exp[-0.0101(T - 273.15)^2 - 0.8525(T - 273.15) + 0.7667] \quad (2.50)$$

for $T \in [239, 255]$ K, and

$$\eta_{\text{dep,s}}(T) = \exp\{46.021(ss_{\text{ice}} - 1)^{\frac{1}{4}} \cdot \cos[0.011(T - 248.560)]^2 \cdot \text{arccot}[0.148(T - 237.570)]/\pi\} \quad (2.51)$$

for $T \in [195, 235]$ K.

ss_{ice} denotes the ice supersaturation and is assumed to be 1.15, for moderate supersaturation conditions in ice clouds (Mamouri and Ansmann, 2016).

Since the continental aerosol surface area concentration is used for the calculation of $n_{\text{INP},s}$, even though it usually includes contributions of continental aerosol other than soot, the result is to be interpreted only as a rough estimate. The INP potential of the cases presented in this work was tested for temperatures of $T = 253.15$ and 243.15 K for immersion freezing, and $T = 228.15$ and 218.15 K for deposition freezing.

In general, both $n_{\text{CCN},i}$ and $n_{\text{INP},i}$ come along with rather high relative uncertainties greater than factor 2. An overview of the relative uncertainties of each of the derived quantities talked about in this section is given in Tab. 2.3.

Parameter		Relative uncertainty
Backscatter coefficient	β_d	10 - 15 %
	β_{nd}	10 - 15 %
	β_m	20 %
	β_c	10 - 20 %
Extinction coefficient	α_d	15 - 25 %
	α_m	25 %
	α_c	20 - 30 %
Mass concentration	M_i	30 - 50 % ¹
Number concentration	$n_{50,i,dry}$	Factor of 1.5 - 2
	$n_{100,i,dry}$	Factor of 1.5 - 2
	$n_{250,i,dry}$	30 - 50 %
Surface area concentration	$s_{i,dry}$	30 - 50 %
CCN number concentration	$n_{CCN,i}$	Factor of 2 - 3
INP number concentration	$n_{INP,i}$	Factor of 3 - 10

Table 2.3: Typical uncertainty ranges of the various aerosol properties. Adapted from Mamouri and Ansmann (2016).

¹ (Ansmann et al., 2012)

3 Measurement campaigns

3.1 CyCARE

3.1.1 Overview

The CyCARE (Cyprus Clouds Aerosol and Rain Experiment) campaign is a collaboration of the Cyprus University of Technology (CUT), Limassol, and Leibniz Institute for Tropospheric Research (TROPOS), Leipzig. It was initiated in order to study the role of different aerosol types on cloud and rain formation, and provide the foundation for an improved understanding of the future development of rain patterns and the effects of climate change in arid regions (Leibniz Institute for Tropospheric Research, 2018a). From October 2016 to March 2018, continuous measurements were performed by the Leipzig Aerosol and Cloud Remote Observations System (LACROS) in Limassol, depicted in Fig. 3.1. The field site was located at 34.675°N , 33.043°E , at the southshore of Cyprus, and 22 m above sea level. Local time is UTC+2. Besides the portable multiwavelength Raman-polarisation lidar Polly^{XT} (shortly described in Sect. 3.1.2), which provided the measurements analysed in this work, a cloud radar, a disdrometer, a Doppler lidar, and a microwave radiometer were installed to provide observations of cloud and precipitation properties, aerosol and cloud dynamics as well as water vapor and liquid water. In Fig. 3.2, all measurement days of Polly^{XT} are shown. Despite some malfunctions, which prohibited measurements on certain days, two precipitation seasons were fully covered, therefore providing a lot of data for further cloud and rain studies.

The CyCARE field campaign also overlapped with measurements performed during the A-LIFE campaign in the same region.

3.1.2 Polly^{XT}

Polly^{XT} is the second generation of portable Raman lidar systems (Polly) with eXTended capabilities. As a so-called 3+2+2+1+2 lidar it determines backscatter coefficients at the wavelengths of 1064 nm, 532 nm, and 355 nm and the extinction coefficients at 532 nm and 355 nm. Additionally, it has two depolarisation channels, one water vapor channel and two receiver units for near-range signals at 532 nm and 355 nm. The vertical and temporal resolution of the raw data is 7.5 m and 30 s, respectively, for all channels (Baars et al., 2016). Engelmann et al. (2016) provide a more detailed description of Polly^{XT}.

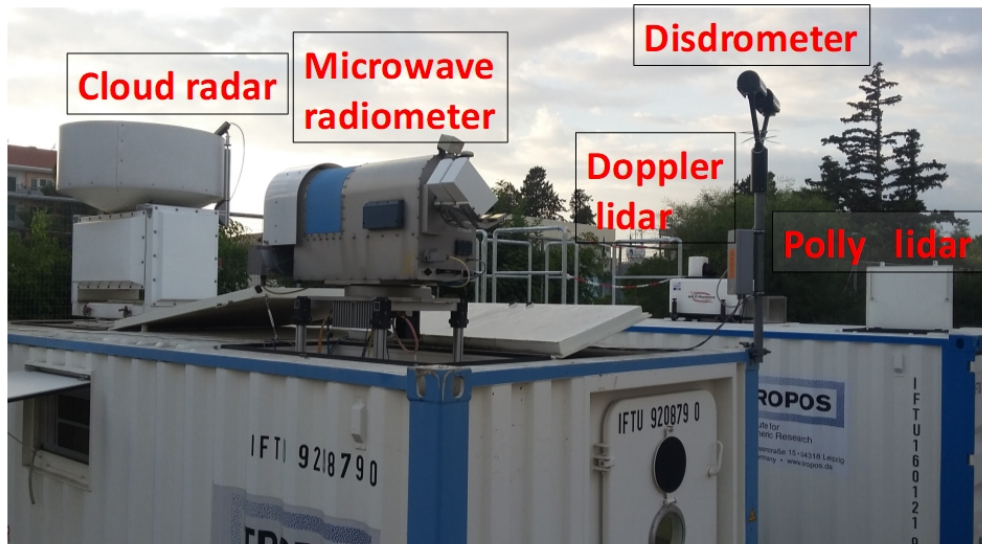


Figure 3.1: The measurement systems of LACROS, deployed in Limassol. (Picture provided by TROPOS)

Okt 2016:	All	20	21	22	23	24	25	26	27	28	29	30	31																			
Nov 2016:	All	01	02	03	04	05	06	07	08	09	10	11	12	13	14	15	16	17	18	19	20	21	22	23	24	25	26	27	28	29	30	
Dez 2016:	All	01	02	03	04	05	06	07	08	09	10	11	12	13	14	15	16	17	18	19	20	21	22	23	24	25	26	27	28	29	30	31
Jan 2017:	All	01	02	03	04	05	06	07	08	09	10	11	12	13	14	15	16	17	18	19	20	21	22	23	24	25	26	27	28	29	30	31
Feb 2017:	All	01	02	03	04	05	06	07	08	09	10	13	14	15	16	17	18	19	20	21	22	23	24	25	26	27	28					
Mär 2017:	All	01	02	03	04	05	06	07	08	10	11	12	13	14	15	16	17	18	19	20	21	22	23	24	25	26	27	28	29	30	31	
Apr 2017:	All	01	02	03	04	05	06	07	08	09	10	11	12	13	14	15	16	17	18	19	20	21	22	23	24	25	26	27	28	29	30	
Mai 2017:	All	01	02	03	04	05	06	07	08	09	10	11	12	13	14	15	16	17	18	19	20	21	22	23	24	25	26	27	28			
Jul 2017:	All	26	27	28	29	30																										
Aug 2017:	All	01	02	03	04	05	06	07	08	09	10	11	12	13	14	15	16	17	18	19	20	21	22	23	24	25	26	27	28	29	30	31
Sep 2017:	All	01	02	03	04	05	06	07	08	09	10	11	12	13	14	15	16	17	18	19	20	21	22	23	24	25	26	27	28	29	30	
Okt 2017:	All	01	02	03	04	05	06	07	08	09	10	11	12	13	14	15	16	17	18	19	20	21	22	23	24	25	26	27	28	29	30	31
Nov 2017:	All	01	02	03	04	05	06	07	08	09	10	11	12	13	14	15	16	17	18	19	20	21	22	23	24	25	26	27	28	29	30	
Dez 2017:	All	01	02	03	04	05	06	07	08	09	10	11	12	13	14	15	16	17	18	19	20	21	22	23	24	25	26	27	28	29	30	31
Jan 2018:	All	01	02	03	04	05	06	07	08	09	10	11	12	13	14	15	16	17	18	19	20	21	22	23	24	25	26	27	28	29	30	31
Feb 2018:	All	01	02	03	04	05	06	07	08	09	10	11	12	13	14	15	16	17	18	19	20	21	22	23	24	25	26	27	28			
Mär 2018:	All	01	02	03	04	05	06	07	08	09	10	11	12	13	14	15	16	17	18	19	20	21	22	23	24	25	26	27				

Figure 3.2: Dates of Polly^{XT} measurements during CyCARE (Leibniz Institute for Tropospheric Research, 2018b).

3.2 A-LIFE

A-LIFE (Absorbing aerosol layers in a changing climate: LIFETIME and dynamics) is an ERC project at the University of Vienna, involving 20 partners from several European countries and the U.S., that started in October 2015 and will last until September 2020. Similarly to CyCARE, this campaign's goal is to investigate the properties of aerosol but with a focus on absorbing aerosols, in particular mineral dust – black carbon mixtures, to gain new understanding of absorbing aerosol layers in the climate system and information for addressing the benefits of black carbon emission controls for mitigating climate change (University of Vienna, 2018c).

A central part of A-LIFE is an aircraft field experiment in the Eastern Mediterranean that took place between 3 and 29 April 2017 with base in Paphos, Cyprus. For the sampling flights, the German Aerospace Center (DLR) research aircraft Falcon was equipped with a suite of in-situ instruments for the determination of microphysical and optical aerosol properties. A full list of the airborne instrumentation is presented in Tab. 3.1. Fig. 3.3 shows an overview of the total flight path, which also included the chasing of a dust outbreak moving eastward towards Cyprus on 19 April 2017. Tab. 3.2 lists the take-off and landing times as well as the main objectives of the respective Falcon flights performed during April 2017.

Furthermore, ground-based instruments were deployed at Paphos airport and Limassol, including sun photometers, a POLIS (PORTable Lidar System) and a trace gas monitor (University of Vienna, 2018b).

Preliminary results for number concentrations of particles with at least 280 nm radius, and up to 25 μm radius, as measured by the Cloud and Aerosol Spectrometer (CAS), have been provided by the University of Vienna for this work, allowing for a comparison of in-situ results with lidar derived ones.

3 Measurement campaigns

Instrument	Measured parameters
Condensation Particle Counters (CPC), 3 CPCs with different lower cut-off, 1 reference CPC for CCN measurements	Total number concentration of fine mode particles ($0.005 \mu\text{m} < D_p < 2.5 \mu\text{m}$) and non-volatile particle fraction
Two Optical Particle Counters (OPC), type Grimm Sky 1.129	Total and non-volatile size distribution ($0.25 \mu\text{m} < D_p < 2.5 \mu\text{m}$)
Thermo-denuder (255°C) + (CPC and OPC)	Total and non-volatile size distribution ($0.01 \mu\text{m} < D_p < 2.5 \mu\text{m}$)
Envitech Optical Particle Analyzer (OPA)	Simultaneous measurement of particle size distribution ($0.5 \mu\text{m} < D_p < 5 \mu\text{m}$) and complex refractive index (660 and 808 nm)
Aerodyne Cavity Attenuated Phase Shift single scattering albedo (CAPS PM _{ssa})	Extinction and scattering coefficient (630 nm), single scattering albedo
Polar nephelometer, type Ecotech Aurora 4000	Particle light scattering coefficient at three wavelengths (450, 525, 635 nm). Light scattering coefficients will be recorded for total scattering and hemispheric backscattering.
Two Brechtel tri-color absorption photometer (TAP)	Absorption coefficient of total aerosol and of sub-micron aerosol at three wavelengths (467, 528, 652 nm)
Three wavelength Particle Soot Absorption Photometer (3- λ -PSAP)	Absorption coefficient of non-volatile aerosol at three wavelengths (467, 530, 660 nm)
Single Particle Soot Photometer (SP2)	Refractory black carbon mass in the range 5 - 104 fg, corresponding to an equivalent size range of 80 - 480 nm, single-particle coating thickness, mixing state
Dual Column Cloud Condensation Nuclei Counter (CCNC)	Number concentration of cloud condensation nuclei at various supersaturations
Impactor sampler	Chemical composition and shape of particles $< 2.5 \mu\text{m}$
Ultra-high Sensitivity Aerosol Spectrometer – Airborne (UHSAS-A)	Aerosol size distributions ($0.06 \mu\text{m} < D_p < 1 \mu\text{m}$)
Passive Cavity Aerosol Spectrometer Probe (PCASP-100X)	Dry state accumulation mode ($0.12 \mu\text{m} < D_p < 3.5 \mu\text{m}$)
Cloud and Aerosol Spectrometer with Detector for Polarisation Detection (CAS-DPOL)	Aerosol particle and cloud hydrometeor size distributions ($0.5 \mu\text{m} < D_p < 50 \mu\text{m}$), particle optical properties, particle shapes
Second generation Cloud, Aerosol, and Precipitation Spectrometer with Polarisation Detection (CAPS)	Aerosol particle and cloud hydrometeor size distributions ($0.5 \mu\text{m} < D_p < 930 \mu\text{m}$), particle optical properties, particle shapes, liquid water content, aircraft velocity
2- μm pulsed Doppler wind lidar	Vertically resolved horizontal wind vector (conical scan), vertical wind speed (nadir pointing), and backscatter coefficient (conical scan and nadir pointing)
Falcon nose boom instrumentation	Position, temperature, pressure, humidity, 3D-wind

Table 3.1: List of instruments aboard the DLR Falcon for A-LIFE. D_p indicates the particle diameter (University of Vienna, 2018b).



Figure 3.3: Total flight path (red) of DLR Falcon during April, 2017. (Picture provided by TROPOS)

3 Measurement campaigns

Date	Take-off (UTC)	Landing (UTC)	Objective
03/04/2017	06:08 (DE)	09:01 (IT)	Transfer flight
03/04/2017	12:38 (IT)	15:49 (CY)	Transfer flight
05/04/2017	08:50 (CY)	12:08 (CY)	Arabian dust
06/04/2017	04:30 (CY)	08:05 (CY)	Arabian (low altitudes) and Saharan dust (higher altitudes)
11/04/2017	05:04 (CY)	08:56 (CY)	Dust in the Cyprus area
11/04/2017	09:56 (CY)	12:59 (CY)	Dust in the Cyprus area
13/04/2017	08:27 (CY)	11:46 (CY)	Dust embedded in clouds
14/04/2017	04:07 (CY)	07:58 (GR)	Dust and pollution sampling over Crete
14/04/2017	09:03 (GR)	12:24 (CY)	Dust and pollution sampling over Crete
19/04/2017	09:58 (CY)	13:56 (MT)	Beginning of a Saharan dust outbreak, which moved eastwards
19/04/2017	15:10 (MT)	19:06 (CY)	Beginning of a Saharan dust outbreak, which moved eastwards
20/04/2017	10:06 (CY)	13:34 (GR)	Maximum of the Saharan dust outbreak
20/04/2017	14:40 (GR)	18:33 (CY)	Maximum of the Saharan dust outbreak
21/04/2017	11:48 (CY)	16:01 (CY)	Dust sampling west and southwest of Cyprus: end of Saharan dust outbreak
22/04/2017	06:07 (CY)	09:26 (CY)	Dust sampling south of Cyprus: end of Saharan dust outbreak
25/04/2017	08:03 (CY)	10:20 (CY)	Sampling of pollution from Turkey and the Black Sea
26/04/2017	12:06 (CY)	14:39 (CY)	Arabian and Saharan dust outbreak
27/04/2017	07:13 (CY)	10:18 (CY)	Arabian and Saharan dust outbreak
29/04/2017	07:06 (CY)	10:34 (GR)	Transfer flight; Saharan dust outbreak
29/04/2017	11:42 (GR)	14:48 (DE)	Transfer flight

Table 3.2: Overview of DLR Falcon flights performed during April 2017. The airport location is indicated in paranthesis: DE corresponds to Oberpfaffenhofen, Germany, IT to Cagliari, Italy, CY to Paphos, Cyprus, GR to Heraklion, Greece, and MT to Malta. Adapted from University of Vienna (2018a).

4 Case studies

Out of the comprehensive ground-based lidar-measurements performed during April 2017 in Limassol, Cyprus, three days with observed dust outbreaks and mostly cloud-free conditions were chosen for thorough analysis with regard to both optical and microphysical properties. For each day two measurement periods were analysed: one during the night to make use of the Raman-lidar method, providing independent backscatter and extinction coefficients as well as lidar ratios, and one during daytime, when sampling flights of A-LIFE took place. The lidar ratios assumed for the latter are based on aerosol optical depth (AOD) comparisons with AERONET data (NASA Goddard Space Flight Center, 2018) of the respective period.

4.1 06 April 2017

The first presented case involves measurements of 06 April 2017. An overview of the atmospheric conditions of the chosen night-time period, 00:00 - 03:00 UTC, in the form of a time-height profile of the range-corrected lidar signal at 1064 nm, is shown in Fig. 4.1. There, two distinct layers of increased signal are visible. Layer 1 ranging up to about 1200 m and layer 2 between 2000 - 4000 m, broadening up to 4500 m by the end of the displayed interval. The time period of the automatic depolarisation calibration, as described by Freudenthaler et al. (2009), (02:30 - 02:40 UTC) is excluded as the lidar signal is being intentionally altered during this time.

The HYSPLIT backward trajectory model, provided by the NOAA Air Resources Laboratory (NOAA Air Resources Laboratory, 2018), was used to identify the origin of both airmasses (Fig. 4.2). Both backward trajectories of layer 2 (2500 m, blue, and 4500 m, green) accredit the respective airmasses a long residence time above the Saharan desert albeit always at altitudes greater than 2000 m, thus preventing a direct dust uptake. In contrast, the corresponding trajectory of layer 1 (500 m, red) shows a path originating in Eastern Europe and going South to Iraq/Jordan, where the airmass got close to the ground, before reaching Cyprus from the southeast. Hence, desert dust particles are to be expected in this layer as well as some marine contribution.

Fig. 4.3 shows the vertical profiles of backscatter and extinction coefficients, lidar ratio, Ångström exponent, and depolarisation ratio calculated for this first night-time period. Vertical smoothing lengths of 187.5 m were used for the backscatter coefficients and depolarisation ratios, and 742.5 m for all other profiles, in order to reduce signal noise.

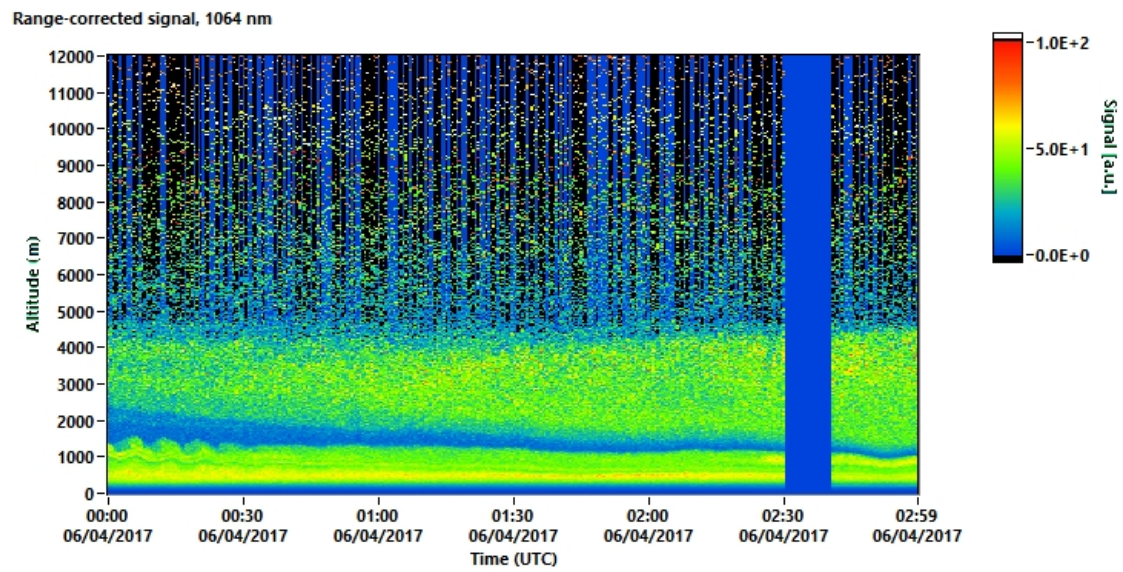


Figure 4.1: Time-height plot of the range-corrected signal at 1064 nm, retrieved on 06 April 2017, 00:00 - 03:00 UTC at Limassol, Cyprus. The period of the automatic daily depolarisation calibration (indicated by the blue bar) was excluded from the calculation of averaged vertical profiles.

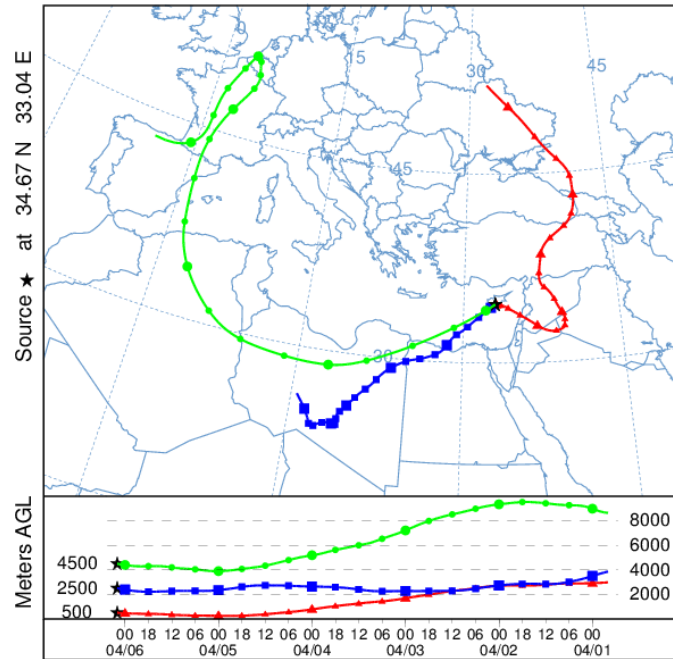


Figure 4.2: 5-day NOAA HYSPLIT backward trajectories of airmasses at 500 (red), 2500 (blue), and 4500 m (green) altitude, arriving in Limassol, Cyprus, on 06 April 2017, 02:00 UTC (NOAA Air Resources Laboratory, 2018).

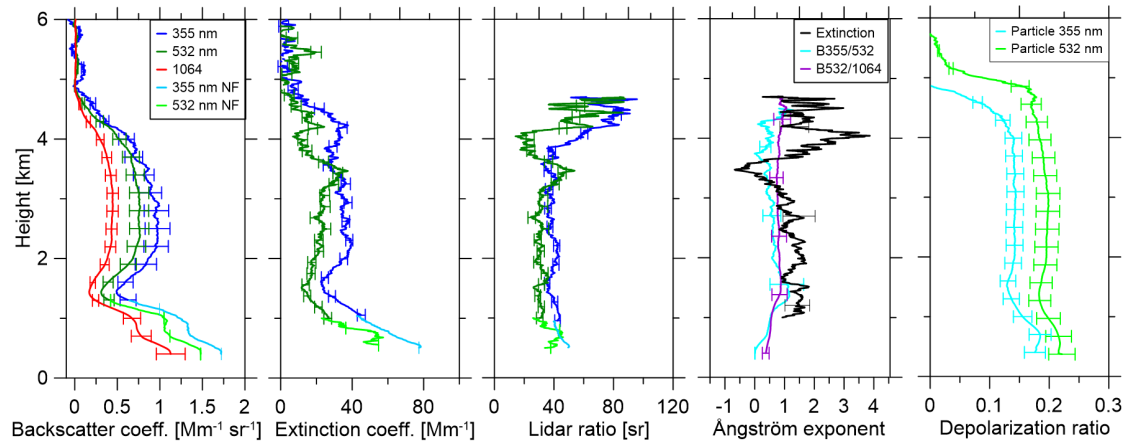


Figure 4.3: Averaged profiles of backscatter and extinction coefficient, lidar ratio, Ångström exponent and particle depolarisation ratio for the period of 06 April 2017, 00:00 - 03:00 UTC at Limassol, Cyprus. Backscatter coefficients and depolarisation ratios are vertically smoothed with 187.5 m; extinction coefficients, lidar ratios, and Ångström exponents with 742.5 m.

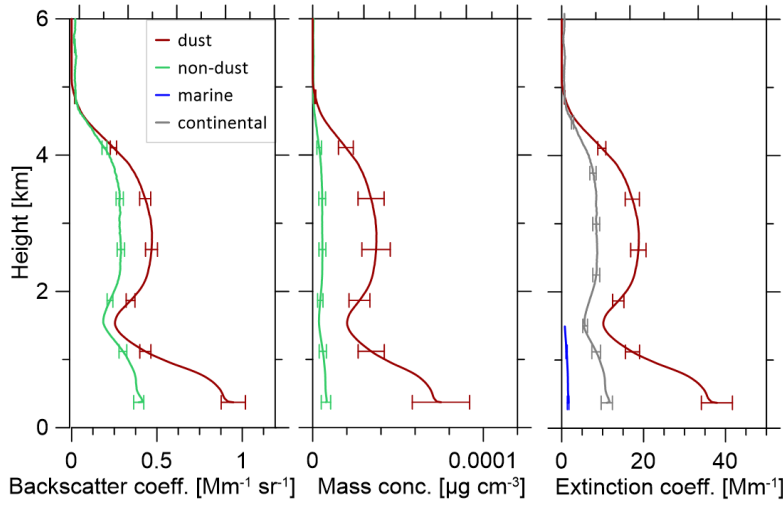


Figure 4.4: Vertical profiles of aerosol-type-dependent backscatter coefficients (left), mass concentrations (middle), and extinction coefficients (right). The total 532 nm particle backscatter coefficient profile of 06 April 2017, 00:00 - 03:00 UTC at Limassol, Cyprus, served as input after a vertical smoothing of 742.5 m had been applied. Used lidar ratios are 40 sr for dust, 30 sr for non-dust, 20 sr for marine, and 35 sr for continental aerosol.

Both layers show similar values of the intensive optical properties. Layer 1 is characterised by lidar ratios of 45 ± 6 sr and 38 ± 5 sr at 355 nm and 532 nm, respectively, indicating a mixture of marine with other particles. Low backscatter-related Ångström exponents of 0.2 ± 0.1 for 355/532 nm wavelength and 0.5 ± 0.02 for 532/1064 nm, as well as particle depolarisation ratios of 19 ± 3 % (355 nm) and 21 ± 3 % (532 nm) additionally suggest the presence of dust particles in this layer.

The second layer (2000 - 4000 m) averages out at lidar ratios of 39 ± 5 sr (355 nm) and 38 ± 5 sr (532 nm). While these values are right in the range of the findings of Nisantzi et al. (2015) for Middle Eastern dust (33–48 sr) and below those of pure Saharan dust (43–65 sr), backward trajectories rather suggest a mixture of Saharan dust with continental aerosol. The extinction-related Ångström exponent takes values of 1.1 ± 0.7 and the backscatter ones of 0.7 ± 0.2 (355/532 nm) and 0.8 ± 0.03 (532/1064 nm). With 14 ± 1 % (355 nm) and 19 ± 2 % (532 nm) the particle depolarisation ratios are a bit lower than those of the lower layer, and support the idea of mixed aerosol types.

In Fig. 4.4, the results of the POLIPHON method (see Sect. 2.5.1), applied to the 532 nm backscatter coefficient and particle depolarisation ratio profile of this case, are presented. Lidar ratios of 40 sr for desert dust, 30 sr for non-dust, 20 sr for marine, and 35 sr for continental aerosol were applied since they produced the best match of the resulting extinction coefficient profile and the measured one, as explained in Sect. 2.5.1.

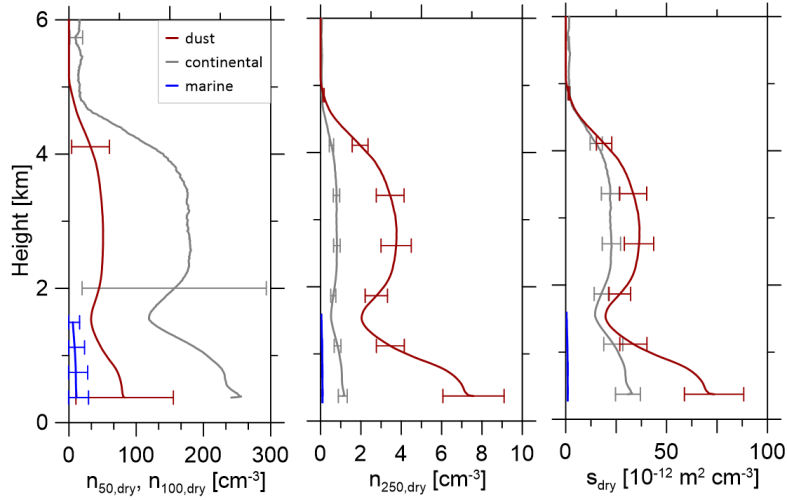


Figure 4.5: Vertical profiles of the number concentrations of particles with dry radius > 50 nm, in the case of marine and continental aerosol, and > 100 nm, in the case of desert dust, (left panel), as well as of particles with dry radius > 250 nm (middle panel) and surface area concentrations (right panel), derived via Eq. 2.34-2.42 from the particle-type-dependent extinction coefficient profiles of 06 April 2017, 00:00-03:00 UTC.

Furthermore, a smoothing length of 742.5 m was applied. The separated backscatter coefficients (left panel) show a higher dust contribution for layer 1 (2.3:1; dust:non-dust) than for layer 2 (1.67:1; dust:non-dust). Mass concentrations of dust range up to $75 \mu\text{g m}^{-3}$ in layer 1 and up to $40 \mu\text{g m}^{-3}$ in layer 2. In the right panel, the corresponding extinction coefficients, with non-dust contribution further distinguished into marine and continental aerosol, are shown.

The respective particle number and surface area concentrations are depicted in Fig. 4.5. For smaller particle radii ($n_{50,\text{dry}}, n_{100,\text{dry}}$, left panel), the continental aerosol number concentration dominates with up to 260 cm^{-3} in layer 1 and 180 cm^{-3} in layer 2, while particles of at least 250 nm radius ($n_{250,\text{dry}}$, middle panel) are mainly desert dust with number concentrations of up to 7 cm^{-3} (layer 1) and 4 cm^{-3} (layer 2). Overall, $n_{250,\text{dry}}$ are at least two orders of magnitude smaller than $n_{50,\text{dry}}, n_{100,\text{dry}}$, since such larger particles are more prone to gravitational sedimentation.

With regard to surface area concentrations, s_{dry} (right panel), the contribution by dust particles ($70 \times 10^{-12} \text{ m}^2 \text{ cm}^{-3}$ in layer 1, and $40 \times 10^{-12} \text{ m}^2 \text{ cm}^{-3}$ in layer 2) is again greater than that of continental aerosol ($35 \times 10^{-12} \text{ m}^2 \text{ cm}^{-3}$ in layer 1, and $25 \times 10^{-12} \text{ m}^2 \text{ cm}^{-3}$ in layer 2) in both layers. As mentioned in Sect. 2.5.3, these values are relevant for the subsequent calculation of INP number concentrations.

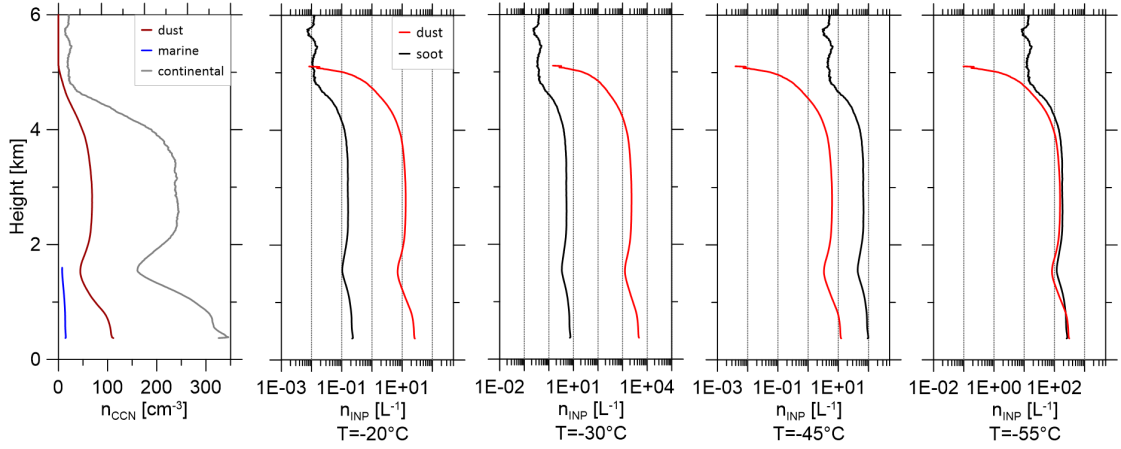


Figure 4.6: Vertical profiles of estimated CCN number concentrations, following Eq. 2.43-2.45 at an assumed supersaturation of 0.25 % (left), as well as INP number concentrations, as derived using Ullrich et al. (2017)’s parameterisations for immersion freezing ($T=-20^{\circ}\text{C}$ and -30°C) and deposition freezing ($T=-45^{\circ}\text{C}$ and -55°C), for the period of 06 April 2017, 00:00-03:00 UTC. Relative uncertainties are typically in the range of factor 2-3 for n_{CCN} , and of factor 3-10 for n_{INP} .

Fig. 4.6 shows the derived cloud relevant parameters. CCN number concentrations n_{CCN} (left panel) are reflective of the previously shown $n_{50,\text{dry}}$, $n_{100,\text{dry}}$, and range up to 350 cm^{-3} (layer 1) and 250 cm^{-3} (layer 2) for continental, and 115 cm^{-3} (layer 1) and 90 cm^{-3} (layer 2) for desert dust. The small marine contribution in the lower layer translates to 15 cm^{-3} on average. Using the enhancement factors mentioned in Sect. 2.5.3, the total maximum n_{CCN} of about 480 cm^{-3} in layer 1 translates to about 600 cm^{-3} at 0.4 % supersaturation. Andreae (2009) analysed a large number of CCN concentration measurements and found averages of $107\pm 56\text{ cm}^{-3}$ for remote marine regions, $200\pm 90\text{ cm}^{-3}$ for remote continental regions, $1060\pm 400\text{ cm}^{-3}$ for polluted marine regions, and $2900\pm 2800\text{ cm}^{-3}$ for polluted continental regions, at 0.4 % supersaturation. Hence, the total maximum CCN number concentration of this case is slightly below the average for polluted marine regions.

The remaining four panels show n_{INP} for temperatures of -20 , -30 , -45 , and -55°C . As mentioned in Sect. 2.5.3, the former two were calculated via the parameterisation for immersion freezing, and the latter two via the one for deposition freezing. Since the best matching lidar ratio of continental aerosol was comparatively low with 35 sr, the soot portion of it is assumedly rather low. Therefore, the resulting soot n_{INP} should be considered only as rough estimates. Pure soot would likely result in higher number concentrations of INP since a greater lidar ratio would increase the related extinction coefficient and with it the $s_{\text{c,dry}}$, from which $n_{\text{INP},s}$ are calculated.

At -20 and -30 °C, the concentration of dust-related INP is about two orders of magnitude higher than soot-related INP, with values of up to 20 L^{-1} in layer 1 and up to 14 L^{-1} in layer 2 at -20 °C, and up to 4000 L^{-1} in layer 1 and up to 3200 L^{-1} in layer 2 at -30 °C. In the range of deposition freezing, at -45 °C, the soot INP concentration is about one order of magnitude higher than the dust INP concentration, with up to 100 L^{-1} in layer 1 and up to 80 L^{-1} in layer 2. At -55 °C, $n_{\text{INP,d}}$ increase significantly up to 230 L^{-1} in layer 1 and up to 200 L^{-1} in layer 2, sharing the maximum values of $n_{\text{INP,s}}$ for this case.

All in all, the INP number concentrations increase with decreasing temperature in the respective heterogeneous freezing regimes. Mineral dust provides more INP for immersion freezing, whereas soot is more efficient in the case of deposition freezing. However, at -55 °C, the difference is only marginal.

The sampling flight with DLR Falcon took place between 04:30 and 08:05 UTC on 06 April. In order to exclude clouds, only the time period of 06:00-08:05 UTC was analysed. During this period, only weak changes in the range-corrected signal at 1064 nm occurred (see Fig. 4.7). Both layers, that were identified during the night, still exist. Layer 2 now consistently spans between 2000-4500 m altitude.

The corresponding profiles of optical properties are shown in Fig. 4.8. A vertical smoothing length of 367.5 m was applied to all profiles. Lidar ratios of 39 sr (355 nm) and 44 sr (532 nm) were assumed as they result in the best AOD match with AERONET data. The extinction-related Ångström exponent yields 0.5 ± 0.2 in layer 1 and 0.4 ± 0.2 in layer 2. Backscatter-related Ångström exponents are 0.9 ± 0.4 (355/532 nm) and 0.3 ± 0.01 (532/1064 nm) in the lower layer, and 0.6 ± 0.4 (355/532 nm) and 0.5 ± 0.02 (532/1064 nm) in the lofted layer. These values generally agree with results of Tesche et al. (2011) for dust-smoke mixtures.

The depolarisation ratio is also very similar to the night-time measurement with 14 ± 1 % at 355 nm and 20 ± 2 % at 532 nm both in layer 1 and the main part of layer 2 (2000-4000 m). However, in the upper part of layer 2 (4000-4500 m) it decreases slightly to 11 ± 1 % at 355 nm and 17 ± 2 % at 532 nm, indicating the presence of more spherical particles.

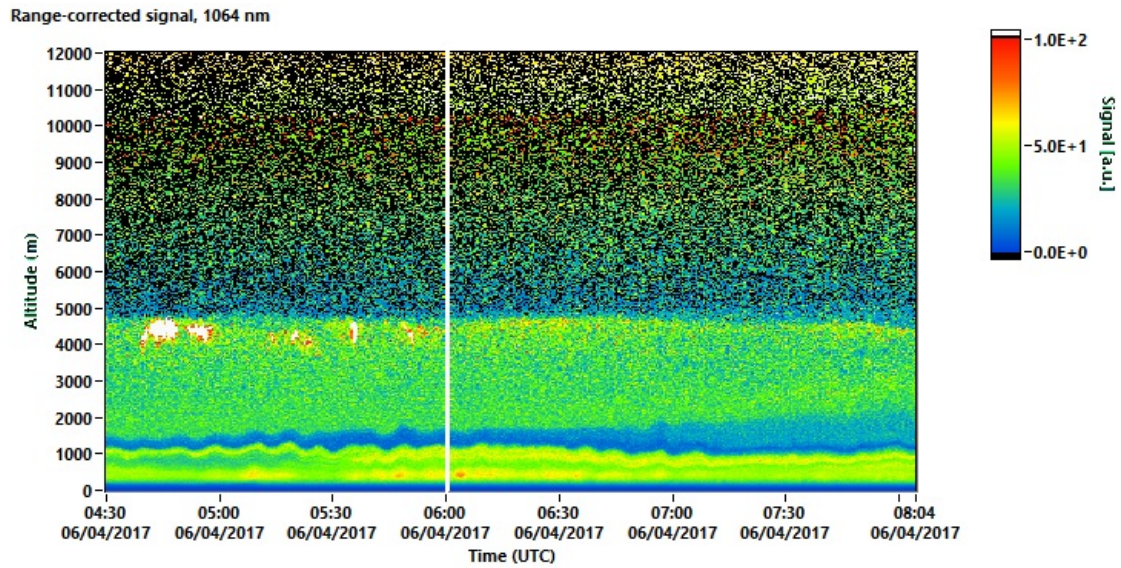


Figure 4.7: Time-height plot of the range-corrected signal at 1064nm, retrieved on 06 April 2017, 04:30-08:05 UTC at Limassol, Cyprus. In order to exclude clouds, only the time period of 06:00-08:05 UTC was analysed.

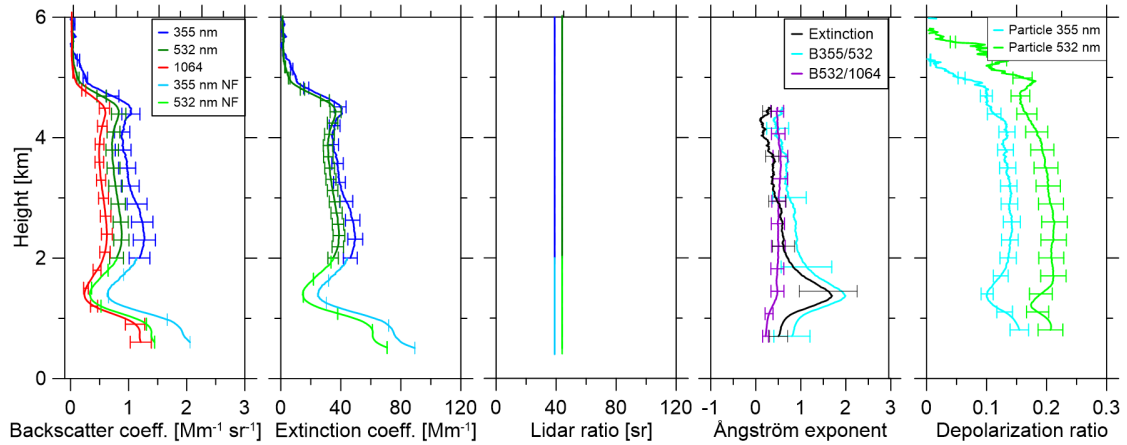


Figure 4.8: Averaged profiles of backscatter and extinction coefficient, Ångström exponent and particle depolarisation ratio for the period of 06 April 2017, 06:00-08:05 UTC at Limassol, Cyprus. Lidar ratios of 39 sr for 355 nm and 44 sr for 532 nm were assumed. The vertical smoothing length for all profiles is 367.5 m.

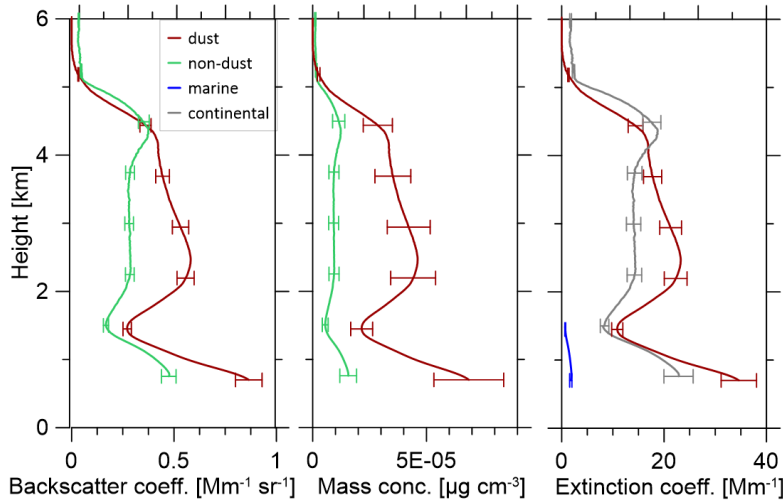


Figure 4.9: Same as Fig. 4.4 but for 06 April 2017, 06:00 - 08:05 UTC. Used lidar ratios are 40 sr for dust, 50 sr for non-dust, 20 sr for marine, and 60 sr for continental aerosol.

Analogically to Fig. 4.4, the separated backscatter and extinction coefficients as well as mass concentrations are depicted in Fig. 4.9. In this case, lidar ratios of 40 sr for dust, 50 sr for non-dust, 20 sr for marine, and 60 sr for continental aerosol were used, the latter indicating a much larger soot portion than during the night. While the desert dust contribution dominates in the majority of the backscatter profile, above 4000 m the non-dust portion increases noticeably and peaks around 4500 m.

The mass concentration of dust remains approximately the same as during the nighttime period in layer 1 but has increased slightly to $45 \mu\text{g m}^{-3}$ in the lower part of layer 2. The non-dust mass concentration has almost doubled, reaching maximum values of $18 \mu\text{g m}^{-3}$ in both layers.

The extinction coefficient profile also reflects the higher portion of continental aerosol particles as only below 1000 m and between 1500 - 4000 m dust makes up the bulk of the overall extinction.

Fig. 4.10 shows the corresponding particle number and surface area concentrations. Again, the number concentration of continental aerosol is a lot larger than that of mineral dust regarding small particles ($n_{50,\text{dry}}, n_{100,\text{dry}}$), with up to 470 cm^{-3} and up to 390 cm^{-3} in layer 1 and layer 2, respectively. Larger particles, $n_{250,\text{dry}}$, are still mostly dust, and its maximum values remain unchanged with 7 cm^{-3} (layer 1) and 5 cm^{-3} (layer 2). s_{dry} however are a lot closer for dust and continental. Both range up to $68 \times 10^{-12} \text{ m}^2 \text{ cm}^{-3}$ in layer 1. Dust holds a higher surface area concentration in the lower part of layer 2 ($50 \times 10^{-12} \text{ m}^2 \text{ cm}^{-3}$) while in the upper part continental aerosol takes higher values ($52 \times 10^{-12} \text{ m}^2 \text{ cm}^{-3}$).

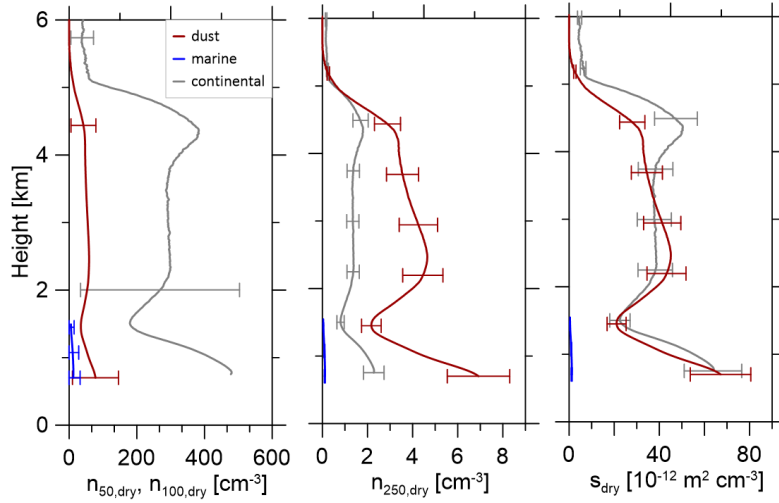


Figure 4.10: Same as Fig. 4.5 but for 06 April 2017, 06:00–08:05 UTC.

The derived n_{CCN} and n_{INP} are given in Fig. 4.11. CCN have increased for each aerosol type with new maximum values of 640 cm^{-3} in layer 1 and 455 cm^{-3} in layer 2 for continental, and 105 cm^{-3} in layer 1 and 95 cm^{-3} in layer 2 for dust. The marine CCN concentration now averages 20 cm^{-3} in the lower layer. The total maximum of about 765 cm^{-3} in layer 1 at 0.25% supersaturation, translates to about 960 cm^{-3} at 0.4% supersaturation, i.e. right in the range of the polluted marine average ($1060 \pm 400 \text{ cm}^{-3}$) found by Andreae (2009).

n_{INP} generally show the same patterns as before in the cases of immersion freezing temperatures. For deposition freezing, soot now clearly dominates at both temperatures. Furthermore, peak values and their allocation with regard to altitude have changed here as well. $n_{INP,d}$ now holds up to 24 L^{-1} in layer 1 and up to 17 L^{-1} in layer 2, at -20°C , and up to 4200 L^{-1} in layer 1 and up to 2800 L^{-1} in layer 2, at -30°C . While $n_{INP,s}$ is about one order of magnitude larger than $n_{INP,d}$ at -45°C (up to 190 L^{-1} in layer 1, up to 117 L^{-1} in layer 2), at -55°C , its maxima of about 530 L^{-1} in both layers only exceed $n_{INP,d}$ by 200 L^{-1} (layer 1) and 300 L^{-1} (layer 2).

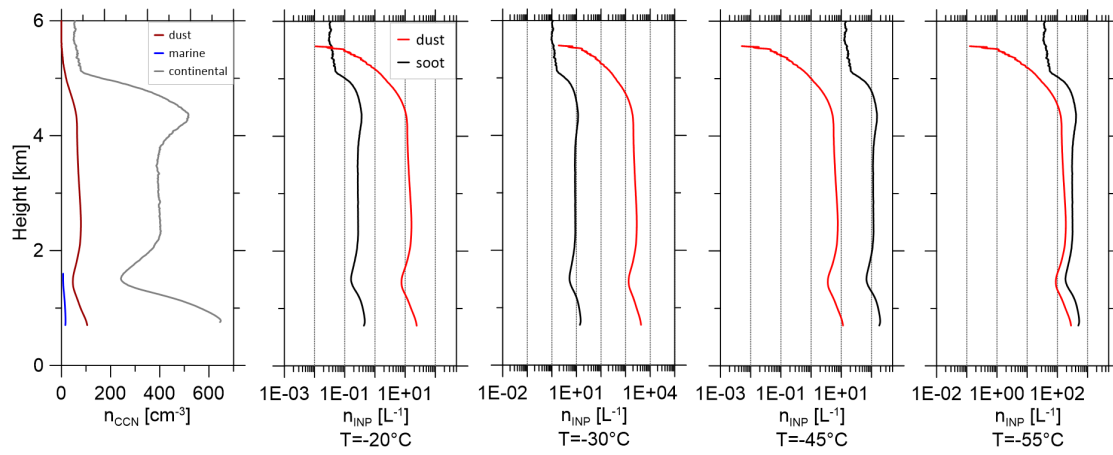


Figure 4.11: Same as Fig. 4.6 but for 06 April 2017, 06:00 - 08:05 UTC.

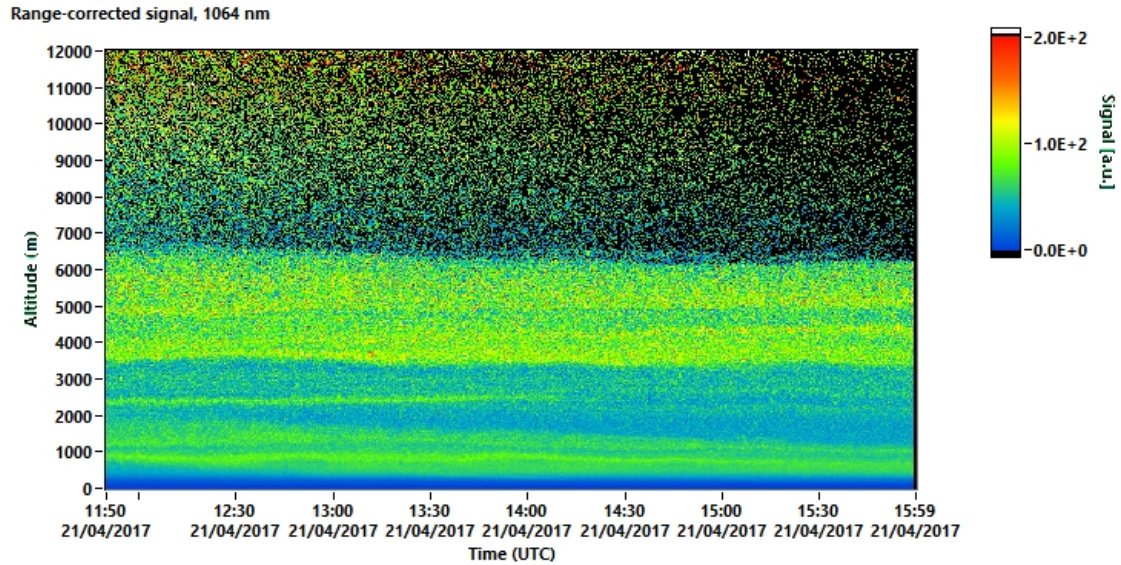


Figure 4.12: Time-height plot of the range-corrected signal at 1064 nm, retrieved on 21 April 2017, 11:50-16:00 UTC at Limassol, Cyprus.

4.2 21 April 2017

Measurements of 21 April 2017 were chosen for the second case study. Between 11:48 and 16:01 UTC, the DLR Falcon sampled dust mainly west and south-west of Cyprus. In Fig. 4.12, the relevant time period is shown by a time-height profile of the range-corrected lidar signal at 1064 nm as it was measured in Limassol. Additionally to the PBL, ranging up to 1700 m, an increased signal can be observed at altitudes around 4000 m and 5500 m, respectively. The corresponding 7-day HYSPLIT backward trajectories, ending at 16:00 UTC, are given in Fig. 4.13. The lowermost airmass (500 m, red) was simulated to have spent the entire past week close to the sea surface, and got close to the shores of Egypt and Lebanon/Israel. In contrast to this, both of the lofted layers originated in the western Sahara, where the middle airmass (4000 m, blue) was also quite close to the ground, allowing for dust uptake. Meanwhile, the uppermost layer (5500 m, green) never got below 2000 m altitude but was, for about 5 days, close enough to the layer below that turbulent mixing could allow for a quite high particle load.

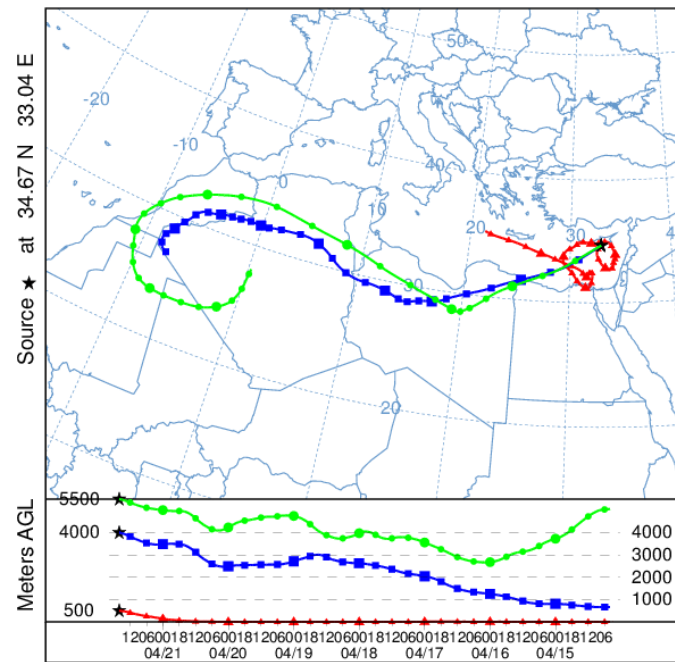


Figure 4.13: 7-day NOAA HYSPLIT backward trajectories of air masses at 500 (red), 4000 (blue), and 5500 m (green) altitude, arriving in Limassol, Cyprus, on 21 April 2017, 16:00 UTC (NOAA Air Resources Laboratory, 2018).

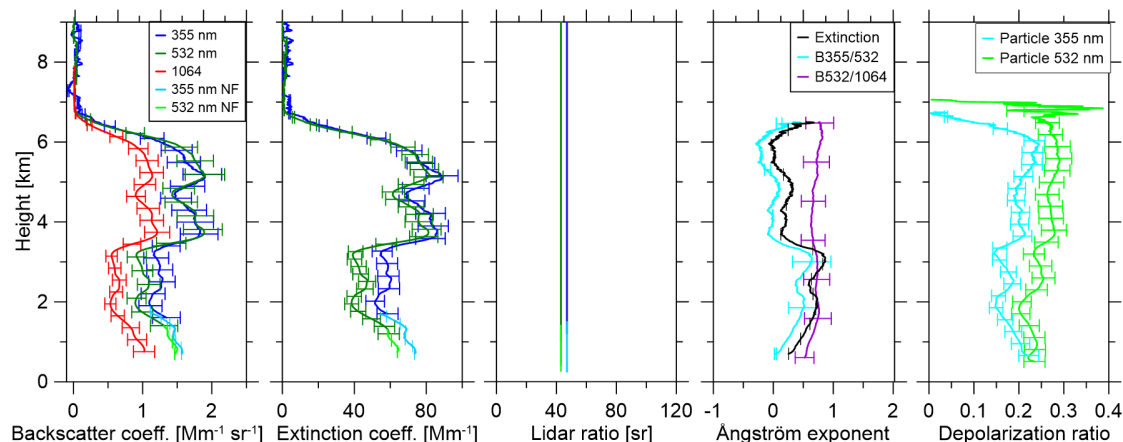


Figure 4.14: Averaged profiles of backscatter and extinction coefficient, Ångström exponent and particle depolarisation ratio for the period of 21 April 2017, 11:50–16:00 UTC at Limassol, Cyprus. Lidar ratios of 47 sr for 355 nm and 43 sr for 532 nm were assumed. The vertical smoothing length for all profiles is 367.5 m.

Fig. 4.14 shows the retrieved vertical profiles of optical properties. For this Klett-retrieval the applied smoothing length was 367.5 m and lidar ratios of 47 sr (355 nm) and 43 sr (532 nm) were assumed.

In the PBL, the extinction-related and the 355/532 nm backscatter Ångström exponent hold average values of 0.5 ± 0.3 and 0.3 ± 0.1 , respectively. The 532/1064 nm backscatter Ångström exponent is slightly higher with 0.6 ± 0.1 . Each of these Ångström exponents is marginally larger than typical values for pure dust, as found by Tesche et al. (2009b). Average particle depolarisation ratios of $19 \pm 2\%$ (355 nm) and $22 \pm 2\%$ (532 nm) indicate the presence of non-spherical mineral dust but also a considerable contribution of spherical, most likely marine, aerosol given the airmass's long residence time right above the Mediterranean. Ångström exponents and depolarisation ratios also point at larger and non-spherical particles at the altitude of 2400 m, between the PBL and the aforementioned lofted layers.

Within the middle layer from 3500–4500 m even lower Ångström exponents of 0.3 ± 0.2 , 0.1 ± 0.05 , and 0.6 ± 0.04 for extinction, 355/532 nm backscatter, and 532/1064 nm backscatter, respectively, were observed, marking wavelength independence of the backscatter signals of 355 and 532 nm. Depolarisation ratios in this height interval are nearly constant and average $20 \pm 2\%$ (355 nm), and $26 \pm 3\%$ (532 nm).

The uppermost layer of 5000–6000 m is characterised by Ångström exponents of 0.1 ± 0.1 (extinction), 0.0 ± 0.05 (355/532 nm backscatter), and 0.8 ± 0.04 (532/1064 nm backscatter), and particle depolarisation ratios of $21 \pm 2\%$ (355 nm), and $29 \pm 3\%$ (532 nm), getting close to typical values of pure dust (about 30%, Groß et al. (2011); Tesche et al. (2011)).

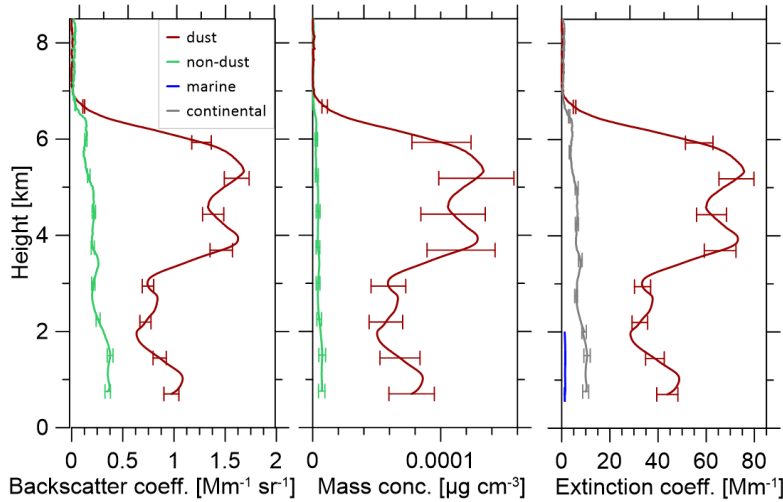


Figure 4.15: Same as Fig. 4.4 but for 21 April 2017, 11:50 - 16:00 UTC. Used lidar ratios are 45 sr for dust, 30 sr for non-dust, 20 sr for marine, and 35 sr for continental aerosol.

For further analysis, again, the 532 nm backscatter signal with smoothing length of 742.5 m was used. Particle-type separated backscatter coefficients, mass concentrations and extinction coefficients are shown in Fig. 4.15. In this case, lidar ratios of 45 sr for dust, 30 sr for non-dust, 20 sr for marine, and 35 sr for continental aerosol were found to match best. The desert dust contribution is in all altitudes a lot larger than the non-desert/marine/continental one. In the PBL, mass concentration of dust peaks at $82 \mu\text{g m}^{-3}$, in the lofted layers even at $128 \mu\text{g m}^{-3}$ (4000 m), and $133 \mu\text{g m}^{-3}$ (5500 m). The non-dust mass concentration decreases almost linearly with height, and holds its maximum of $6 \mu\text{g m}^{-3}$ in the PBL.

Fig. 4.16 illustrates the derived particle number and surface area concentrations for this case. Continental aerosol particles dominate regarding smaller particles ($n_{50,\text{dry}}$, $n_{100,\text{dry}}$) only at lower altitudes, with maximum value of 230 cm^{-3} . In the ranges of the previously identified lofted layers, the smaller dust particles outnumber continental ones, with 130 cm^{-3} at 4000 m, and 135 cm^{-3} at 5500 m. The bulk of $n_{250,\text{dry}}$ stems from dust particles, reaching values of up to 9 cm^{-3} (1100 m), 14 cm^{-3} (4000 m), and 15 cm^{-3} (5500 m). Similarly, s_{dry} are a lot larger for dust than for continental aerosol, translating to maxima of $90 \times 10^{-12} \text{ m}^2 \text{ cm}^{-3}$, $143 \times 10^{-12} \text{ m}^2 \text{ cm}^{-3}$, and $147 \times 10^{-12} \text{ m}^2 \text{ cm}^{-3}$ at 1100, 4000, and 5500 m, respectively.

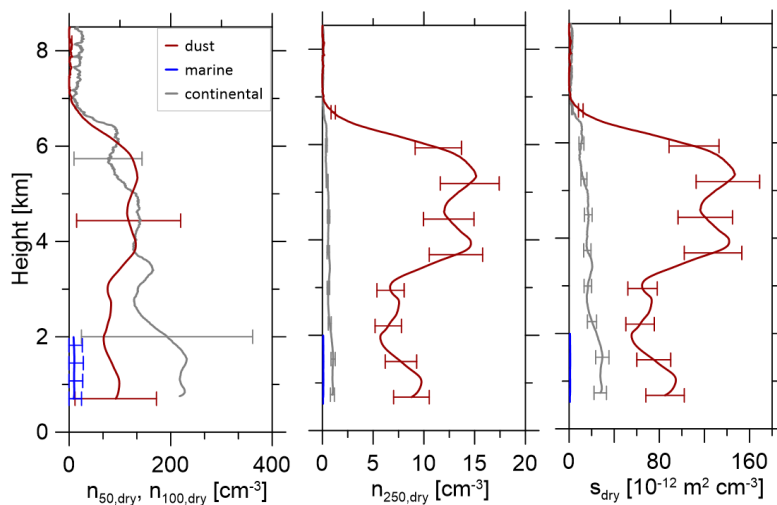


Figure 4.16: Same as Fig. 4.5 but for 21 April 2017, 11:50-16:00 UTC.

Number concentrations of CCN and INP for this case are shown in Fig. 4.17, in the same manner as for 06 April. Dust-related CCN reach number concentrations of 130 cm^{-3} (1100 m), 177 cm^{-3} (4000 m), and 181 cm^{-3} (5500 m). While continental aerosol-related CCN are most numerous in the PBL with up to 307 cm^{-3} , marine particles are estimated to only provide CCN of up to 13 cm^{-3} . Thus, the total maximum of n_{CCN} holds about 450 cm^{-3} at 0.25%, and about 570 cm^{-3} at 0.4% supersaturation, setting this case a bit below Andreae (2009)'s polluted marine region average of $1060 \pm 400\text{ cm}^{-3}$.

Considering the lidar ratio for continental aerosol, similarly to the night-time case of 06 April, a rather low soot contribution is expected, making the calculated number concentrations of soot-related INP again quite a rough estimate. At -20°C , $n_{\text{INP,d}}$ holds values up to 50 L^{-1} in the lofted layers, while $n_{\text{INP,s}}$ is about two orders of magnitude smaller with about 0.2 L^{-1} below 1700 m. The former increases by more than two, and the latter by more than one orders of magnitude for -30°C . The maximum values are 9000 L^{-1} and 6 L^{-1} for dust and soot, respectively.

For deposition freezing, soot initially grants more INP at -45°C with up to 87 L^{-1} versus dust's peak of 24 L^{-1} . However, for a temperature as low as -55°C , dust again dominates in each of the considered layers with up to 610 L^{-1} .

Overall, a lot higher particle load was observed during this period than on 06 April 2017.

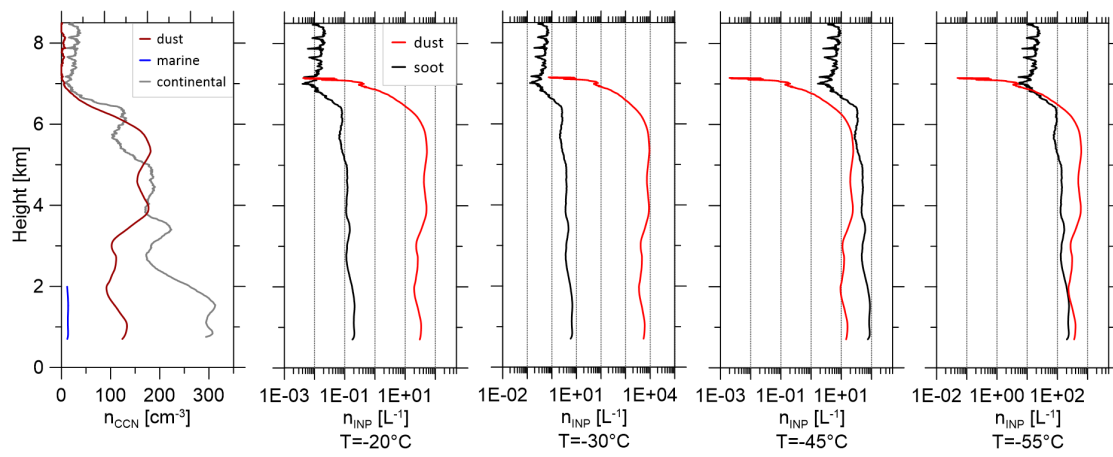


Figure 4.17: Same as Fig. 4.6 but for 21 April 2017, 11:50-16:00 UTC.

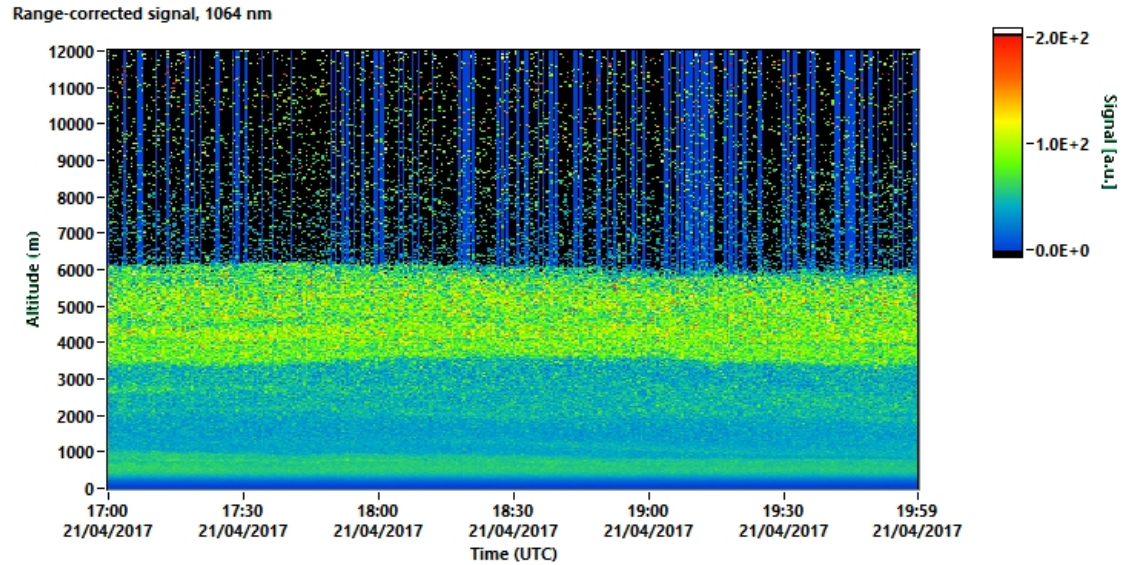


Figure 4.18: Time-height plot of the range-corrected signal at 1064 nm, retrieved on 21 April 2017, 17:00 - 20:00 UTC at Limassol, Cyprus.

In order to supplement the analysis, the time period of 17:00 - 20:00 UTC was also examined. The respective 1064 nm range-corrected signal plot is shown in Fig. 4.18. The previously observed two lofted layers are hardly distinguishable anymore, indicating mixing of the two. Hence, they will be treated as a single layer, ranging from 4000 - 6000 m, in the following.

Fig. 4.19 provides an overview of the backscatter and extinction coefficients, lidar ratios, Ångström exponents and depolarisation ratios, that were calculated from this observation period. Again, a vertical smoothing of 187.5 m was applied to backscatter coefficients and depolarisation ratios, and a smoothing of 742.5 m to the remaining parameters.

In the PBL, up to 1200 m, lidar ratios of 355 and 532 nm are very similar with 39 ± 4 sr and 40 ± 4 sr, respectively. Backscatter-related Ångström exponents average 0.3 ± 0.1 (355/532 nm), and 0.7 ± 0.03 (532/1064 nm). Particle depolarisation ratios are slightly greater than in the previous period with $19 \pm 2\%$ and $22 \pm 2\%$. Overall, these values again indicate a mixture of aerosol types.

Between 4000 - 6000 m, lidar ratios of 60 ± 10 sr (355 nm) and 53 ± 6 sr (532 nm) are in good agreement with previous studies' findings regarding Saharan dust (Groß et al., 2011; Freudenthaler et al., 2009). The backscatter-related Ångström exponents of -0.2 ± 0.1 (355/532 nm), and 0.6 ± 0.03 (532/1064 nm), as well as the, inspite of the applied smoothing, noisy extinction Ångström exponent of 0.1 ± 0.1 confirm the presence of comparatively large particles.

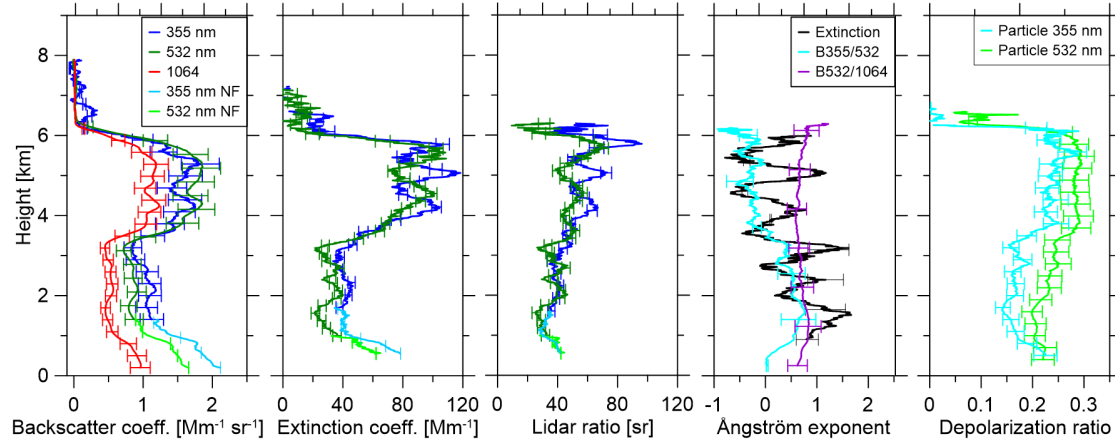


Figure 4.19: Averaged profiles of backscatter and extinction coefficient, lidar ratio, Ångström exponent and particle depolarisation ratio for the period of 21 April 2017, 17:00-20:00 UTC at Limassol, Cyprus. Backscatter coefficients and depolarisation ratios are vertically smoothed with 187.5 m; extinction coefficients, lidar ratios, and Ångström exponents with 742.5 m.

According to Veselovskii et al. (2016), negative Ångström exponents may result from the spectral dependence of the imaginary part of dust’s refractive index. Values of $24 \pm 3\%$ (355 nm) and $28 \pm 3\%$ (532 nm) for the particle depolarisation ratios also indicate a high contribution of mineral dust in this layer.

The particle-type separated backscatter coefficients, mass concentrations, and extinction coefficients for the 532 nm backscatter profile, with smoothing of 742.5 m, were calculated using lidar ratios of 50 sr for dust, 40 sr for non-dust, 20 sr for marine, and 45 sr for continental aerosol. Fig. 4.20 shows the corresponding profiles. The dust portion is quite high, translating to mass concentrations of about $71 \mu\text{g m}^{-3}$ in the PBL and to up to $135 \mu\text{g m}^{-3}$ in the lofted layer. The non-dust contribution initially decreases with height but holds a small maximum just above 6000 m altitude.

Because of the conversion to the continental particle number concentration $n_{50,\text{dry}}$ (see Fig. 4.21, left panel), this peak is enhanced and yields up to 180 cm^{-3} at 6100 m. In the PBL, the concentration of these smaller particles goes up to 400 cm^{-3} . Below 4000 m and above 6000 m, continental aerosol particles contribute the most small particles. In the range of the lofted dust layer, the desert dust portion is only slightly larger than the continental one with up to 145 cm^{-3} . Larger particle number concentrations $n_{250,\text{dry}}$ mostly contain dust, with up to 10 cm^{-3} in the PBL and up to 17 cm^{-3} in the lofted layer, as shown in Fig. 4.21’s middle panel.

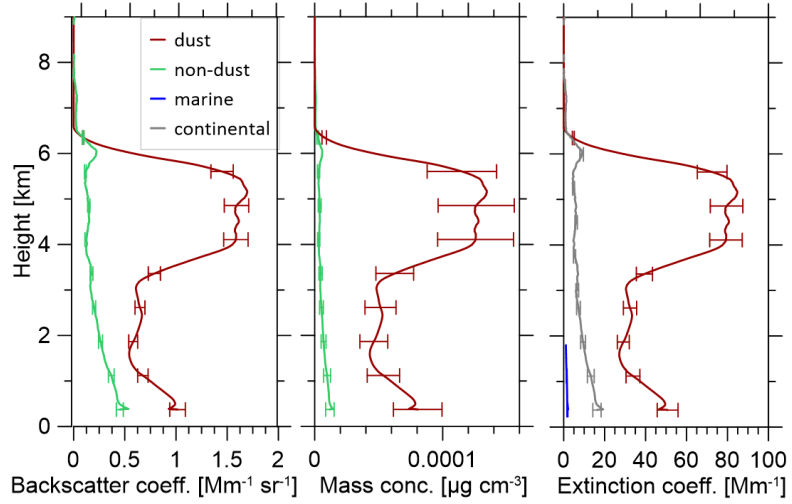


Figure 4.20: Same as Fig. 4.4 but for 21 April 2017, 17:00 - 20:00 UTC. Used lidar ratios are 50 sr for dust, 40 sr for non-dust, 20 sr for marine, and 45 sr for continental aerosol.

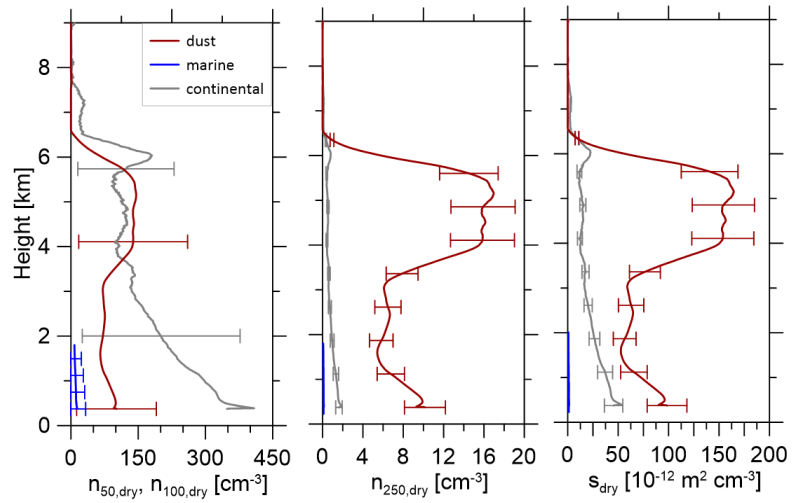


Figure 4.21: Same as Fig. 4.5 but for 21 April 2017, 17:00 - 20:00 UTC.

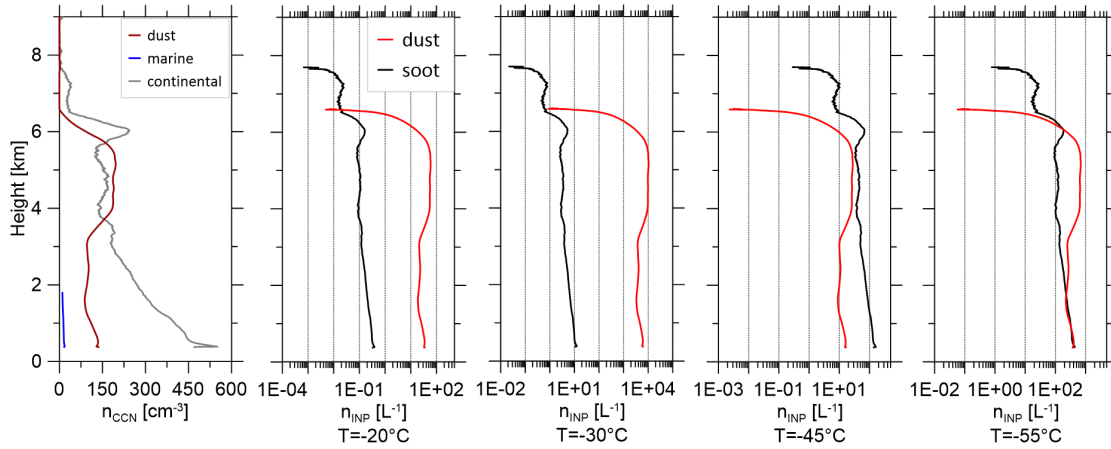


Figure 4.22: Same as Fig. 4.6 but for 21 April 2017, 17:00 - 20:00 UTC.

The corresponding surface area concentrations are depicted in the right panel of Fig. 4.21. The dust-related profile's values are greater at all heights with up to $95 \times 10^{-12} \text{ m}^2 \text{ cm}^{-3}$ (PBL) and up to $170 \times 10^{-12} \text{ m}^2 \text{ cm}^{-3}$ (lofted layer), whereas continental aerosol-related values only range up to about 50 % (PBL) and 15 % (lofted layer) of these concentrations.

Fig. 4.22 shows the finally derived number concentrations of CCN and INP. In the PBL, the maximum $n_{\text{CCN},c}$ now ranges up to 520 cm^{-3} , while $n_{\text{CCN},d}$ only go up to 145 cm^{-3} . Marine particles contribute about 20 cm^{-3} in the PBL. This yields a maximum total CCN number concentration of 685 cm^{-3} at 0.25 %, and about 860 cm^{-3} at 0.4 % supersaturation, which again fits into the average of $1060 \pm 400 \text{ cm}^{-3}$ for polluted marine regions (Andreae, 2009).

INP number concentrations for immersion freezing are again higher for dust than for soot, with maxima of 35 L^{-1} (-20°C , PBL), 60 L^{-1} (-20°C , lofted layer), 6000 L^{-1} (-30°C , PBL), and 9700 L^{-1} (-30°C , lofted layer). While soot and dust maxima occur at different heights, overall the gap between them increases from two orders of magnitude at -20°C to three orders of magnitude at -30°C . At -45°C , soot provides more INP in general. This is more pronounced in the PBL, with 150 L^{-1} versus dust's 16 L^{-1} . Between 4000 - 6000 m, $n_{\text{INP},d}$ comes close to soot values of 30 L^{-1} . For deposition freezing at -55°C , both dust and soot hold about equal n_{INP} in the PBL, with up to 410 L^{-1} . In the lofted layer, soot-related INP are almost an order of magnitude less than dust-related INP, with about 95 L^{-1} and 700 L^{-1} , respectively.

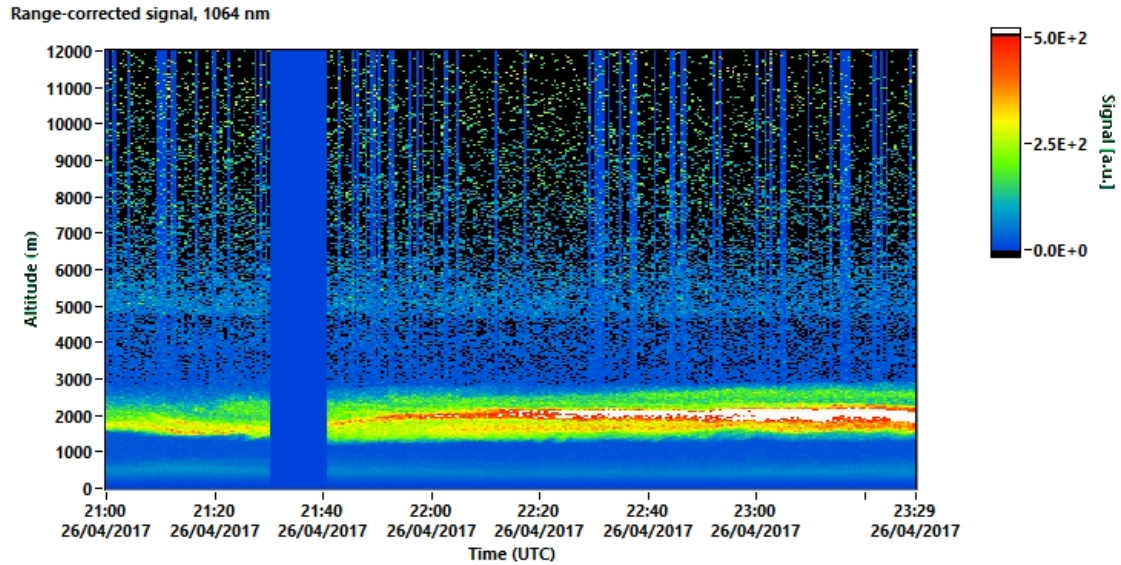


Figure 4.23: Time-height plot of the range-corrected signal at 1064 nm, retrieved on 26 April 2017, 21:00 - 23:30 UTC at Limassol, Cyprus. The period of the automatic daily depolarisation calibration (indicated by the blue bar) was excluded from the calculation of averaged vertical profiles.

4.3 26/27 April 2017

On 27 April 2017, the last sampling flight of A-LIFE took place. The lidar observation on 26 April 2017 from 21:00 - 23:30 UTC was chosen as the related night-time period since the best (highest reaching) profiles could be obtained from this measurement interval. Fig. 4.23 shows the corresponding time-height plot of the range-corrected signal at 1064 nm. Another depolarisation calibration coincided with this period. The respective time interval was again ignored for the purpose of calculating averaged profiles of the different aerosol properties. In Fig. 4.23, a thick aerosol layer, spanning between 1400 - 2800 m altitude, is most prominent. Additionally, the PBL up to 800 m, and another layer around 5000 m can be identified, despite a comparatively much weaker signal. Like in the previous cases, HYSPLIT 5-day backward trajectories, ending at 09:00 UTC in Limassol, were calculated and are shown in Fig. 4.24. The trajectory of the uppermost layer (5000 m, green) originated in Southern Spain and took a comparatively straight path towards Cyprus, passing only shortly above the Algerian and Tunisian coastal areas. Still, it always remained at altitudes greater or close to 5000 m, preventing the take-up of many aerosol particles.

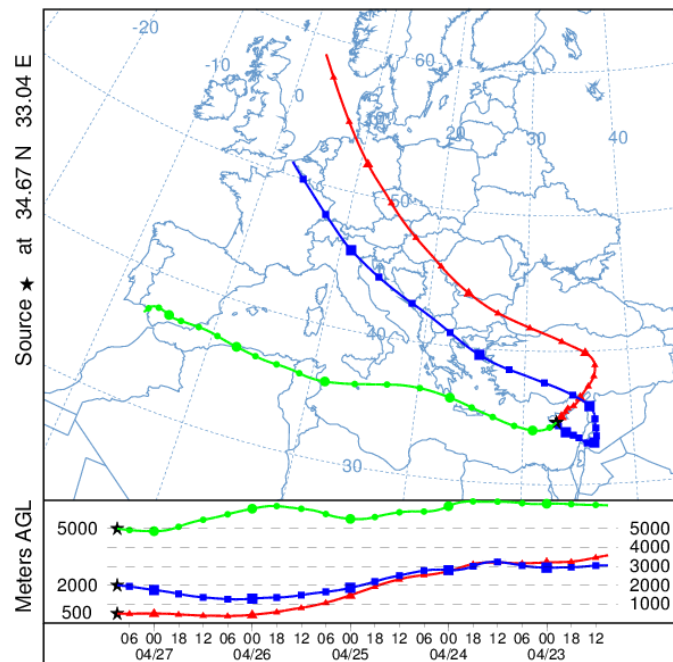


Figure 4.24: 5-day NOAA HYSPLIT backward trajectories of airmasses at 500 (red), 2000 (blue), and 5000 m (green) altitude, arriving in Limassol, Cyprus, on 27 April 2017, 09:00 UTC (NOAA Air Resources Laboratory, 2018).

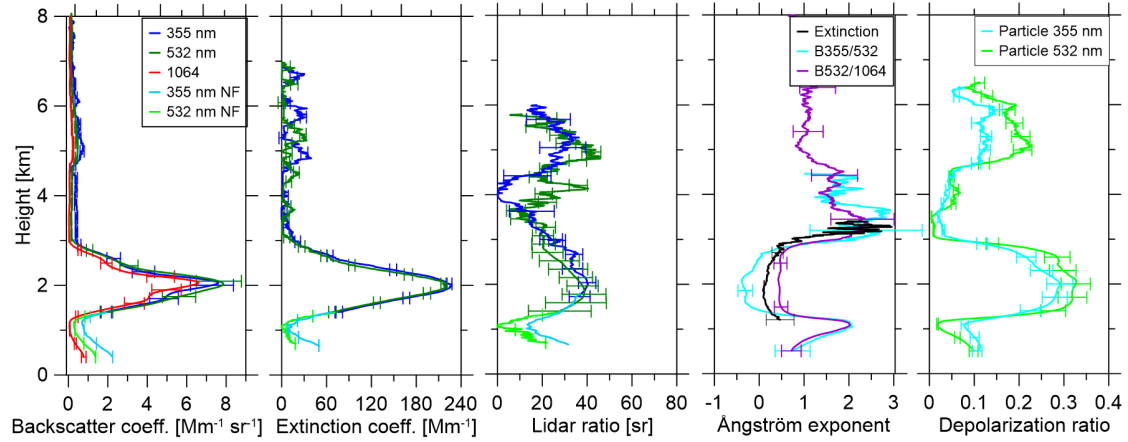


Figure 4.25: Averaged profiles of backscatter and extinction coefficient, lidar ratio, Ångström exponent and particle depolarisation ratio for the period of 26 April 2017, 21:00 - 23:30 UTC at Limassol, Cyprus. Backscatter coefficients and depolarisation ratios are vertically smoothed with 187.5 m; extinction coefficients, lidar ratios, and Ångström exponents with 742.5 m.

The airmasses at 500 m (red) and 2000 m (blue) both traveled south-east above the European continent at very similar altitudes around 3000 m. While the trajectory starting in the PBL got quite close to the ground above Turkey, and turned towards Cyprus from there, the air of the middle layer still remained above 1000 m at all times, and continued its path towards south-east. However, about two days before flowing to Cyprus, the simulated trajectory suggests, that this airmass was at its lowest altitude close to the Middle Eastern desert area, allowing for a heavy dust load.

Fig. 4.25 shows the lidar-derived aerosol optical properties' vertical profiles. Here, a vertical smoothing of 187.5 m was applied to the profiles of backscatter coefficients and depolarisation ratios. The remaining parameters were smoothed with 742 m.

Since the PBL was rather shallow in this case, and profiles were only analysable upward of 500 m, due to incomplete overlap below this height, this layer will not be discussed.

The main layer between 1400 - 2800 m is characterised by lidar ratios of 37 ± 5 sr at 355 nm and 36 ± 4 sr at 532 nm, which fall into the typical range of Middle Eastern dust lidar ratios of 33 - 48 sr, found by Nisantzi et al. (2015). The quasi wavelength independence of extinction coefficients, indicative of the presence of mineral dust (Kanitz et al., 2013), results in an average extinction Ångström exponent of 0.3 ± 0.2 . Backscatter-related Ångström exponents hold values of -0.1 ± 0.1 (355/532 nm) and 0.5 ± 0.06 (532/1064 nm). Particle depolarisation ratios of 26 ± 3 % and 31 ± 3 % at 355 nm and 532 nm, respectively, indicate almost pure dust.

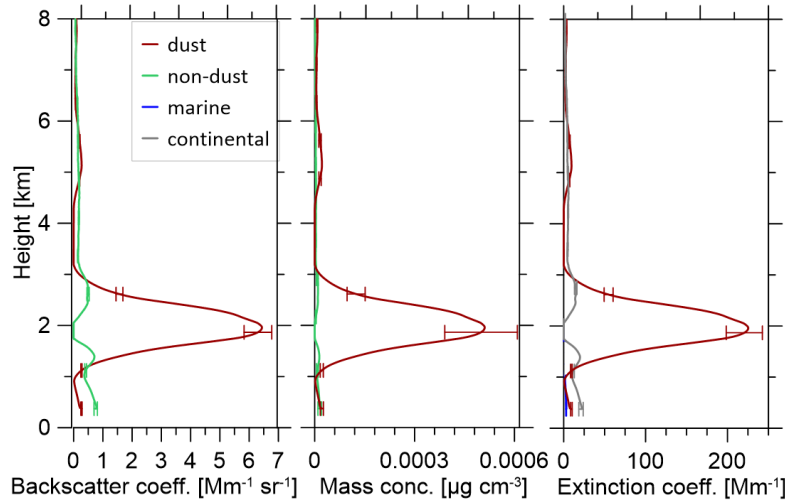


Figure 4.26: Same as Fig. 4.4 but for 26 April 2017, 21:00 - 23:30 UTC. Used lidar ratios are 35 sr for dust, 30 sr for non-dust, 20 sr for marine, and 35 sr for continental aerosol.

Above this layer, the lidar signal is severely weakened, resulting in very noisy lidar ratios of 28 ± 4 sr (355 nm) and 32 ± 4 sr (532 nm) inside the lofted layer (4800 - 6000 m). The backscatter-related Ångström exponent of 532/1064 nm is 1.1 ± 0.2 in this layer and is the only Ångström exponent available at this altitude. In comparison to the main layer, the particle depolarisation ratios are smaller with values of 14 ± 2 % (355 nm) and 20 ± 2 % (532 nm). Overall, in this layer a mixture of mostly continental aerosol and dust is expected albeit at very low concentrations.

In Fig. 4.26, aerosol-type separated 532 nm backscatter coefficients as well as the derived mass concentrations and extinction coefficients are depicted. Lidar ratios of 35 sr for dust, 30 sr for non-dust, 20 sr for marine, and 35 sr for continental aerosol were used. Before the calculation, a smoothing of 742.5 m was applied to the 532 nm backscatter coefficient.

At all heights, except for 1800 - 2000 m, a low non-dust contribution exists. In the pure dust area the mass concentration goes up to $510 \mu\text{g m}^{-3}$. The lofted layer is barely distinguishable with a dust mass concentration maximum of $21 \mu\text{g m}^{-3}$.

Particle number and surface area concentrations are shown in Fig. 4.27. $n_{50,\text{dry}}$, $n_{100,\text{dry}}$ are mostly of continental origin, with maximum values of 430 cm^{-3} and 300 cm^{-3} at the main aerosol layer's lower and upper boundaries. At 2000 m, small dust particles dominate with up to 290 cm^{-3} . Large dust particles hold number concentrations of up to 45 cm^{-3} in the main layer and up to 3 cm^{-3} in the lofted layer. Non-dust $n_{250,\text{dry}}$ are

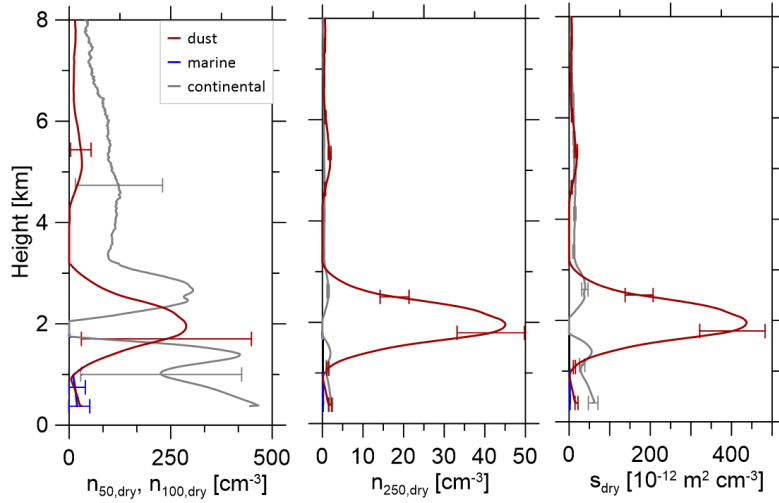


Figure 4.27: Same as Fig. 4.5 but for 26 April 2017, 21:00-23:30 UTC.

consistently below 5 cm^{-3} . Surface area concentrations s_{dry} of dust dominate in the two layers with up to $435 \times 10^{-12} \text{ m}^2 \text{ cm}^{-3}$ (main layer) and up to $18 \times 10^{-12} \text{ m}^2 \text{ cm}^{-3}$ (lofted layer). Outside of those areas a higher contribution stems from continental aerosol particles, though it is quite small in comparison to dust's maxima with up to $47 \times 10^{-12} \text{ m}^2 \text{ cm}^{-3}$ at 700 m.

Fig. 4.28 shows the retrieved n_{CCN} and n_{INP} profiles for this case. Maximum continental CCN number concentrations are 560 cm^{-3} and 400 cm^{-3} at 1500 m and 2800 m, respectively. In general, the continental concentrations are a lot higher, except in the middle of the main layer, where dust particles are the only source of CCN with up to 390 cm^{-3} . The assumed marine contribution translates to approximately 20 cm^{-3} below 1000 m. The total maximum of CCN is located right below the pure dust interval of the main layer, at about 1500 m, and holds about 800 cm^{-3} , or about 1010 cm^{-3} at 0.4% supersaturation. Again, this estimation of CCN number concentration is in line with Andreae (2009)'s average of $1060 \pm 400 \text{ cm}^{-3}$ for polluted marine regions.

INP number concentrations of dust are again greater than soot's in the range of immersion freezing, peaking around 150 L^{-1} (-20°C , main layer), 7 L^{-1} (-20°C , lofted layer), 27500 L^{-1} (-30°C , main layer), and 1000 L^{-1} (-30°C , lofted layer). In contrast, soot-related INP number concentrations only go up to 0.3 L^{-1} at -20°C , and up to 15 L^{-1} at -30°C . At -45°C , soot provides more INP, with up to 180 L^{-1} versus dust's 73 L^{-1} , and 3 L^{-1} in the main and lofted layer, respectively. However, at -55°C , the main layer's dust INP concentration exceeds soot's maxima again by almost a whole order of magnitude, with up to 1800 L^{-1} around 2000 m. In the lofted layer, both dust and soot-related INP are very close with about 90 L^{-1} (dust) and 100 L^{-1} (soot).

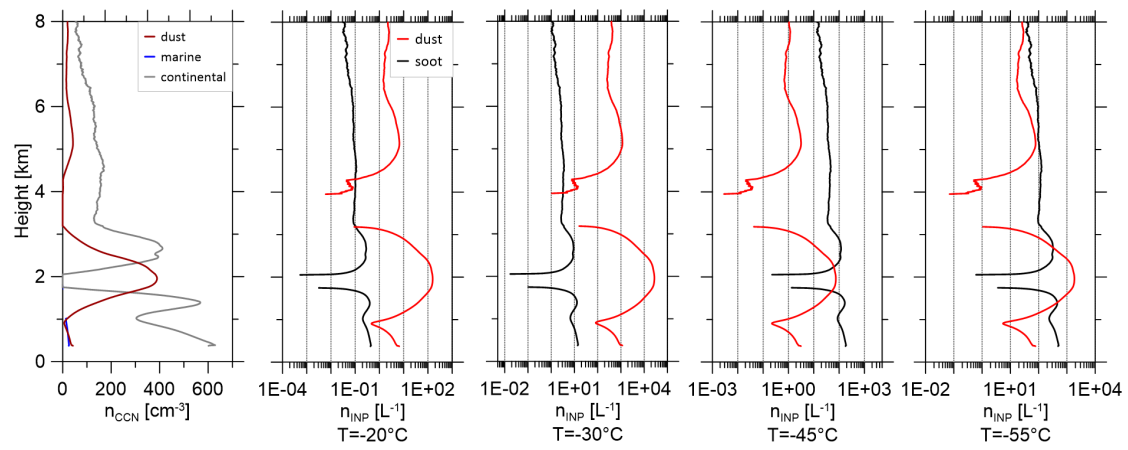


Figure 4.28: Same as Fig. 4.6 but for 26 April 2017, 21:00 - 23:30 UTC.

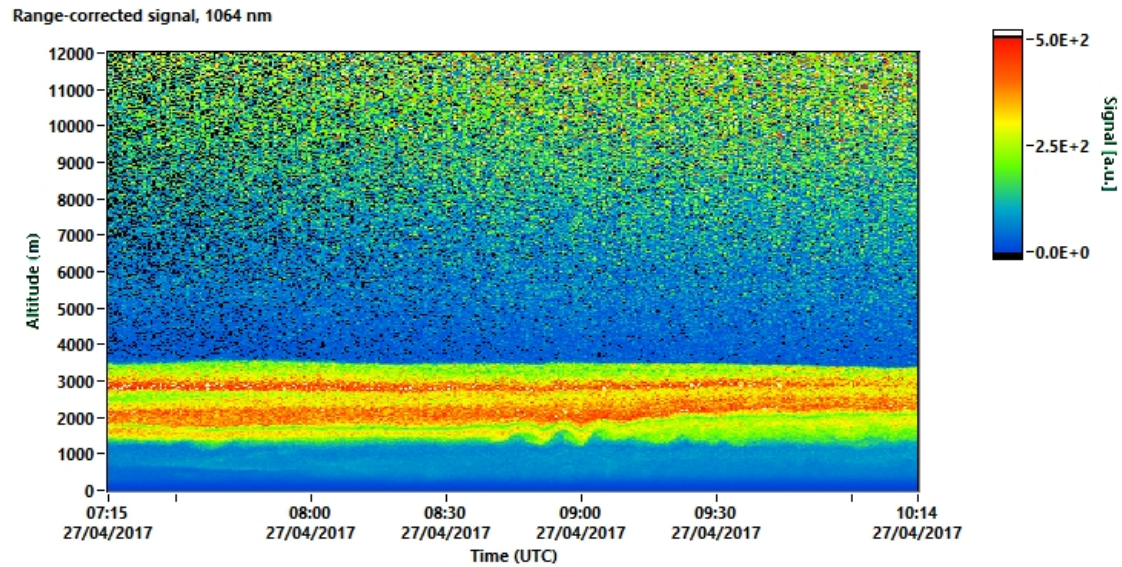


Figure 4.29: Time-height plot of the range-corrected signal at 1064 nm, retrieved on 27 April 2017, 07:15- 10:15 UTC at Limassol, Cyprus.

Since the sampling flight on 27 April lasted from 07:13- 10:18 UTC, the last daytime period to be analysed was chosen to be 07:15- 10:15 UTC. The corresponding 1064 nm range-corrected signal plot is shown in Fig.4.29. Compared to the previous night's observation, the main layer's depth has considerably increased, now ranging from 1500- 3500 m. While in this plot the lofted layer is no longer visible, Fig.4.30's Ångström exponent and particle depolarisation profiles still indicate the presence of particles between 4500- 6000 m. A vertical smoothing length of 367.5 m was applied to all profiles, and lidar ratios of 42 sr for 355 nm, and 38 sr for 532 nm were chosen on the basis of AOD comparison.

In the main layer, Ångström exponents are 0.1 ± 0.1 and -0.1 ± 0.1 for extinction and backscatter 355/532 nm, respectively. The 532/1064 nm backscatter Ångström exponent holds a larger mean of 0.8 ± 0.05 . The calculated particle depolarisation ratios of $27 \pm 3 \%$ at 355 nm and $30 \pm 3 \%$ at 532 nm are typical for almost pure dust (Tesche et al., 2009b).

Between 4500- 6000 m, Ångström exponents of 1.3 ± 0.9 (extinction), 1.2 ± 0.8 (355/532 nm backscatter), and 1.8 ± 0.1 (532/1064 nm backscatter) as well as depolarisation ratios of $15 \pm 2 \%$ (355 nm) and $18 \pm 2 \%$ (532 nm) indicate a dusty mixture of aerosol.

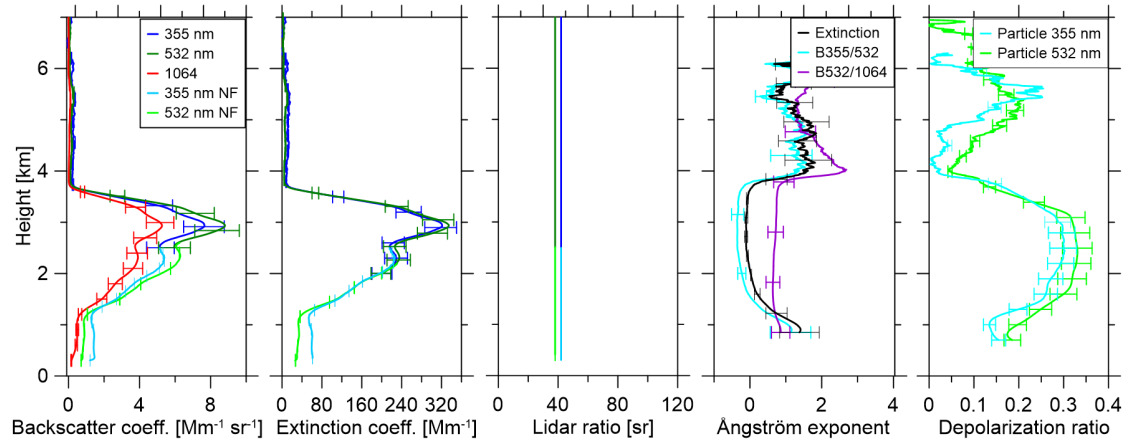


Figure 4.30: Averaged profiles of backscatter and extinction coefficient, Ångström exponent and particle depolarisation ratio for the period of 27 April 2017, 07:15-10:15 UTC at Limassol, Cyprus. Lidar ratios of 42 sr for 355 nm and 38 sr for 532 nm were assumed. The vertical smoothing length for all profiles is 367.5 m.

The separated 532 nm backscatter coefficients, again smoothed with 742.5 m, in Fig. 4.31 indicate equal contributions of dust and non-dust aerosol in the upper layer. In this case, lidar ratios of 38 sr for dust, 30 sr for non-dust, 20 sr for marine, and 35 sr for continental aerosol were used for the subsequent calculations.

The main layer's dust mass concentration goes up to $605 \mu\text{g m}^{-3}$, marking the overall highest dust mass concentration presented in this work. At the upper boundary of this layer, around 3200-3700 m, the highest continental aerosol contribution is located, as is apparent from the separated extinction coefficient profiles.

Fig. 4.32 shows the particle number and surface area concentrations. With regard to small particles $n_{50,\text{dry}}$, $n_{100,\text{dry}}$, the greatest concentration is of continental origin at 3500 m with up to 680 cm^{-3} . Small dust particle number concentrations range up to 340 cm^{-3} in the main layer. The bulk of $n_{250,\text{dry}}$ stems from desert dust particles with up to 58 cm^{-3} . Surface area concentrations peak around $560 \times 10^{-12} \text{ m}^2 \text{ cm}^{-3}$ at 3000 m in the case of dust, and around $95 \times 10^{-12} \text{ m}^2 \text{ cm}^{-3}$ at 3500 m in the case of continental aerosol.

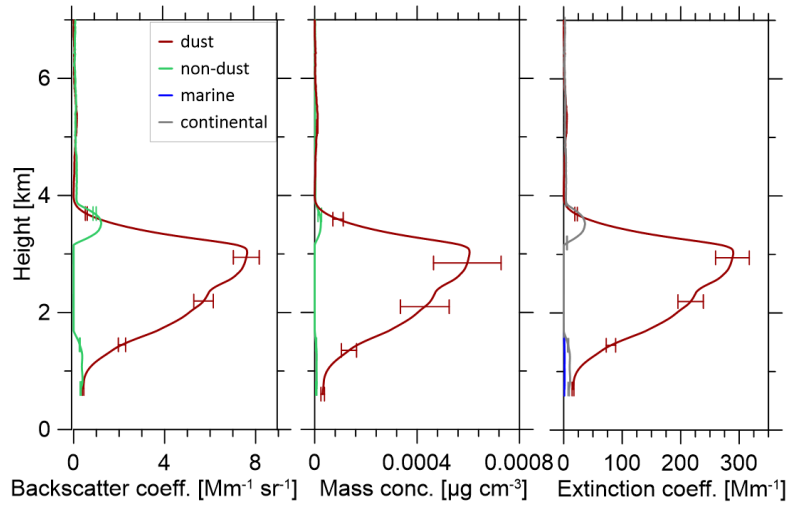


Figure 4.31: Same as Fig. 4.4 but for 27 April 2017, 07:15 - 10:15 UTC. Used lidar ratios are 38 sr for dust, 30 sr for non-dust, 20 sr for marine, and 35 sr for continental aerosol.

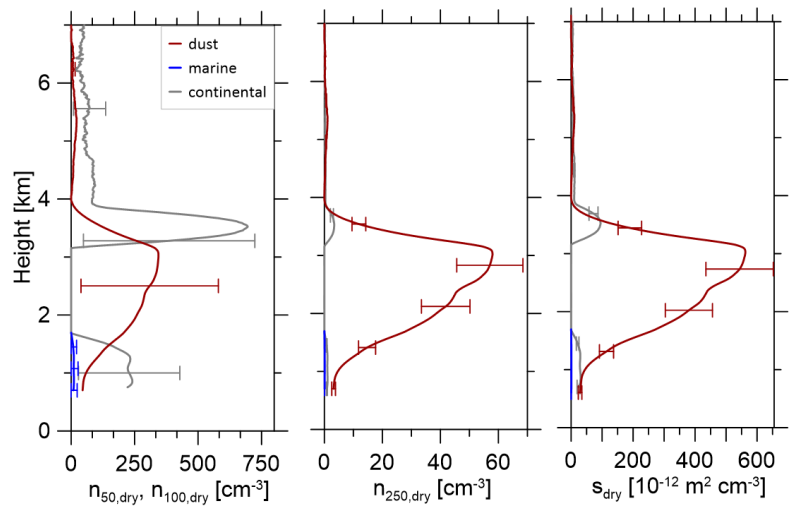


Figure 4.32: Same as Fig. 4.5 but for 27 April 2017, 07:15 - 10:15 UTC.

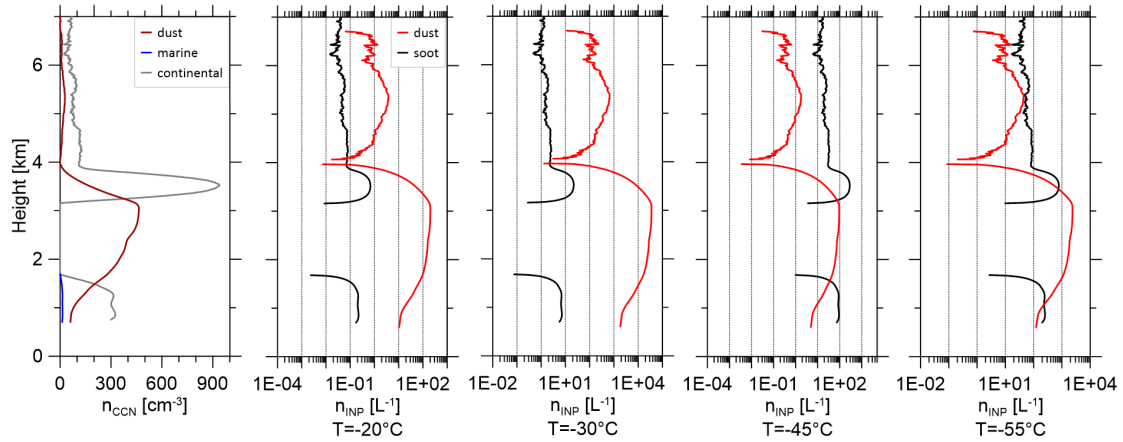


Figure 4.33: Same as Fig. 4.6 but for 27 April 2017, 07:15 - 10:15 UTC.

The corresponding CCN and INP number concentrations are depicted in Fig. 4.33. Below and above the main layer, continental CCN concentrations hold values of up to 350 cm^{-3} and 940 cm^{-3} , respectively. 460 cm^{-3} is the maximum dust-related CCN number concentration at 3000 m. The small marine contribution translates to 14 cm^{-3} . At 3500 m altitude, the total maximum n_{CCN} is 1150 cm^{-3} at 0.25% and about 1450 cm^{-3} at 0.4% supersaturation. This number almost exceeds the polluted marine average of $1060 \pm 400 \text{ cm}^{-3}$ found by Andreae (2009).

At -20°C , maximum $n_{\text{INP},d}$ hold about 200 L^{-1} in the main layer and about 5 L^{-1} in the lofted layer, while $n_{\text{INP},s}$ are significantly lower, only ranging up to 0.7 L^{-1} . This difference increases at -30°C , where $n_{\text{INP},d}$ peaks at 35000 L^{-1} (3000 m) and 660 L^{-1} (5200 m) versus soot's 20 L^{-1} .

The deposition freezing parameterisation yields up to 280 L^{-1} $n_{\text{INP},s}$ at -45°C . Generally, higher number concentrations are estimated for soot than for dust at this temperature. However, in the pure dust range of the main layer, $n_{\text{INP},d}$ peaks at 95 L^{-1} . Dust and soot-related INP concentrations are closest at -55°C . In the main layer the dust profile holds a maximum of 2300 L^{-1} , whereas the soot one goes up to 280 L^{-1} . Between 4500 - 6000 m the n_{INP} 's maxima are 45 L^{-1} (dust) and 90 L^{-1} (soot).

Tab. 4.1 summarises the maximum values of dust and non-dust mass concentrations, dust, marine and continental aerosol-related CCN number concentrations, and dust and soot-related INP number concentrations at -30°C as they were discussed in this chapter, in order to provide an overview of the aerosol load during each of the presented cases.

Date	Period (UTC)	Mass conc.		n_{CCN}			n_{INP} at -30°C	
		dust	non-dust	dust	marine	cont.	dust	soot
06/04/2017	00:00 - 03:00	75	10	115	15	350	4000	9
	06:00 - 08:05	70	18	105	20	640	4200	15
21/04/2017	11:50 - 16:00	133	6	181	13	307	9000	6
	17:00 - 20:00	135	15	145	20	520	9700	12
26/04/2017	21:00 - 23:30	510	7	390	20	560	27500	15
27/04/2017	07:15 - 10:15	605	5	460	14	940	35000	20

Table 4.1: Overview of the maximum values of mass concentration in $\mu\text{g m}^{-3}$, CCN number concentration n_{CCN} in cm^{-3} , and INP number concentration n_{INP} at -30°C in L^{-1} as they were derived from the lidar observation of each time period.

5 Comparison with A-LIFE measurements

As mentioned in the previous chapter, sampling flights of A-LIFE were performed during the already discussed daytime lidar measurement periods. Fig. 5.1 shows the DLR Falcon's flight tracks for each of the days. All of the flights passed over Limassol (marked by the LACROS location on the map) at some point, thereby creating a spatial and temporal overlap of in-situ and lidar measurements. In the case of the flights of 06 and 27 April 2017, the majority of the sampling happened over the Mediterranean south of Limassol and along the southern coastline of Cyprus. In contrast, the flight of 21 April 2017 ranged several hundred kilometers west of Cyprus and passed over the isle of Cyprus in the north of Limassol.

For this comparison, the University of Vienna provided preliminary A-LIFE in-situ results of CAS measurements of the number concentrations of particles with radius > 280 nm (n_{280}) without error estimations. Since the data analysis scheme of Mamouri and Ansmann (2016) only aims at particles with radius > 250 nm, a deviation of in-situ and lidar-based retrieved number concentrations is to be expected.

To roughly compare both Cyprus campaigns' results, the total of the previously shown $n_{250,i,dry}$ was calculated for each case (labeled as calc. $n_{250,total}$) and plotted with the respective CAS measurement (labeled as CAS n_{total}) in Fig. 5.2. In order to obtain data for vertical profiles, the research aircraft flew up and down several times over the course of each pattern, thereby creating a range of datapoints at each height.

For the in-situ measurement of 06 April 2017 (Fig. 5.2, left panel), the calculated $n_{250,total}$ fits quite well for altitudes above 1700 m. Below that height and down until the beginning of incomplete overlap at about 700 m, where the $n_{250,total}$ profile is cut off, $n_{250,total}$ still approximately follows the shape of the CAS measured curve but yields slightly higher particle number concentrations. Since $n_{250,total}$ also includes particles with radius between 250-280 nm, this deviation might be explained by the presence of such smaller particles. This effect, however, should be observable, at least rudimentally, at any height. Therefore, local influences are most likely responsible for the increased $n_{250,total}$ at low altitudes.

The measured n_{280} and calculated $n_{250,total}$ for the case of 21 April 2017 are displayed in the middle panel of Fig. 5.2. The corresponding flight track was the one that ranged farthest away from Limassol, suggesting greater discrepancies between $n_{250,total}$ and CAS n_{total} . Values of $n_{250,total}$ indeed are lower than the measured ones in the observed dust layer above 4000 m. Yet, below this altitude both are in good agreement, except for one large peak in the measurement between 500 and 1000 m.

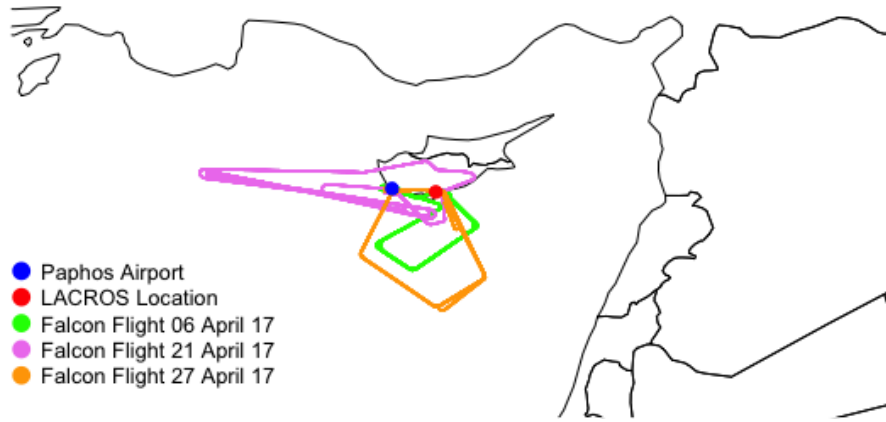


Figure 5.1: Overview of DLR Falcon’s flight tracks on 06 April 2017, 04:30 - 08:05 UTC; 21 April 2017, 11:48 - 16:01 UTC; and 27 April 2017, 07:13 - 10:18 UTC.

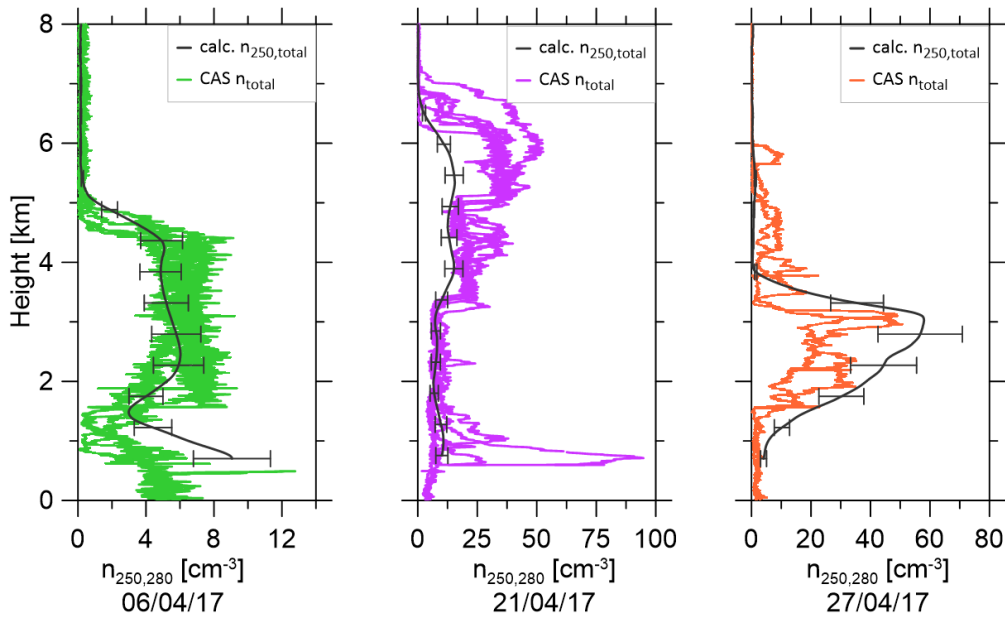


Figure 5.2: Comparison of the sum of the lidar-derived $n_{250,i}$, shown in chapter 4, with preliminary in-situ CAS measurements, provided by A-LIFE’s PI, Bernadett Weinzierl, for each of the three daytime measurement periods.

At the time when this peak was observed, the Falcon's location was at 34.733°N, 31.176°E, i.e. far to the west of the isle of Cyprus. For comparison, the ground-based lidar was located at 34.675°N, 33.043°E. Taking this into account, this peak may be considered negligible in the context of this comparison.

The flight performed on 27 April 2017 (Fig. 5.2, right panel) was the shortest of the ones shown in this work, while ranging the farthest south of Limassol. In the layer between 2000-4000 m and down to 700 m, $n_{250,\text{total}}$ fits the shape of the measured curves relatively well, although with higher number concentration values. However, above 4000 m and up to 6000 m particles were still sampled while $n_{250,\text{total}}$ is close to 0 cm⁻³. Going back to the vertical profiles of optical properties for this case (Fig. 4.30), the depolarisation ratio does exhibit another peak in this height interval, indicating the presence of non-spherical particles. As the underlying main dust layer weakened the signal detected from this altitude, the derived backscatter coefficient is quite uncertain due to the very low signal to noise ratio. Since $n_{250,\text{total}}$ is ultimately derived from the backscatter coefficient, a proper estimation of the particle number concentration at the 4000-6000 m height interval is not possible in this case of stacked aerosol layers.

Still, overall reasonably good agreements between lidar derived and in-situ results were achieved for each case. This is promising for the ongoing closure between lidar and in-situ, which would foster the experimental methods and thus lead to a better understanding of CCN and INP concentration in the atmosphere. This in turn might help to better simulate aerosol-cloud-interactions.

While for this work only preliminary particle number concentration measurements were available, there is potential for a more in-depth comparison in the future as A-LIFE data analysis is still in progress.

6 Conclusion and Outlook

Cyprus is an island heavily affected by a multitude of different types of aerosol such as desert dust, originating from both the Sahara and Middle-Eastern deserts, as well as marine and continental aerosol. Because of this, it provides an interesting field site for studies to improve the understanding of aerosols and aerosol-cloud-interaction.

During the CyCARE campaign on Cyprus from October 2016 to March 2018, the TROPOS' LACROS was deployed in Limassol to accumulate a comprehensive data set, obtained by measurements of the multiwavelength Raman-lidar Polly^{XT}, as well as several other instruments used to study aerosol, clouds and precipitation.

Additionally, airborne in-situ measurements of aerosol were made in the framework of the A-LIFE campaign in April 2017, thereby creating a period of overlap of both Polly^{XT} and in-situ measurements.

In this work, three days involving dust outbreaks over Cyprus were presented and analysed with regard to both aerosol optical properties, i.e. lidar ratios, Ångström exponents, and particle depolarisation ratios, and microphysical properties, i.e. mass, particle number, surface area, CCN and INP number concentrations, following the procedure suggested by Mamouri and Ansmann (2016), aided by use of HYSPLIT backward trajectories (NOAA Air Resources Laboratory, 2018). In contrast to Mamouri and Ansmann (2016), a more recent INP parameterisation, found by Ullrich et al. (2017), was used to derive INP number concentrations in this work. For each case study, one nighttime and one daytime period was chosen in order to make use of the Raman-lidar method's potential for independent extinction coefficients and lidar ratios as well as to provide a comparison to A-LIFE's in-situ measurements, which were only conducted during daytime.

On 06 April 2017, a lofted aerosol layer consisting of a mixture of Saharan dust and smoke was observed. Lidar ratios of 39 ± 5 sr and 38 ± 5 sr at 355 nm and 532 nm, Ångström exponents of 0.4 ± 0.2 (extinction), 0.7 ± 0.2 (355/532 nm backscatter), and 0.8 ± 0.03 (532/1064 nm backscatter) as well as depolarisation ratios of 14 ± 1 % (355 nm) and 19 ± 2 % (532 nm) also agree with the presence of a dusty mixture. In terms of volume composition, this mixture consisted of about 80 % desert dust and 20 % continental aerosol, most likely pollution from Egypt.

A layer of almost pure Saharan desert dust passed over Cyprus on 21 April 2017. The corresponding lidar ratios of 60 ± 10 sr (355 nm) and 53 ± 6 sr (532 nm), Ångström exponents of 0.1 ± 0.1 (extinction), -0.2 ± 0.1 (355/532 nm backscatter), and 0.6 ± 0.03 (532/1064 nm backscatter) as well as depolarisation ratios of 24 ± 3 % (355 nm) and 28 ± 3 % (532 nm) all agree well with previous studies like e.g. Groß et al. (2011) or Nisantzi et al. (2015). The last presented cases were from 26/27 April 2017. In contrast to the aforementioned cases, a very dense layer of mineral dust from the Middle East was observed together with a very thin layer of dust from the Saharan desert. For the Middle Eastern dust layer, lidar ratios of 37 ± 5 sr (355 nm) and 36 ± 4 sr (532 nm), as well as Ångström exponents of 0.3 ± 0.2 (extinction), -0.1 ± 0.1 (355/532 nm backscatter), and 0.5 ± 0.06 (532/1064 nm backscatter) as well as depolarisation ratios of 26 ± 3 % (355 nm) and 31 ± 3 % (532 nm) were found, indicating pure dust. Values of the lofted layer averaged 28 ± 4 sr and 32 ± 4 sr for lidar ratios at 355 nm and 532 nm, respectively. The 532/1064 nm backscatter Ångström exponent was the only available one and held a value of 1.1 ± 0.2 . Furthermore, depolarisation ratios of 14 ± 2 % (355 nm) and 20 ± 2 % (532 nm) indicated a mixture of mostly continental aerosol and dust.

The overall highest particle load, and thus greatest CCN and INP number concentrations were observed on 27 April 2017, while the 06 April 2017 held the lowest concentrations of the presented cases. Additionally, the number concentrations of smaller (CCN-relevant) particles n_{50}, n_{100} were usually highest for continental aerosol, whereas dust-related n_{250} dominated in the range of larger particles. In general, n_{250} were always outnumbered by n_{50}, n_{100} as they are more prone to gravitational sedimentation.

Using the enhancement factors suggested by Mamouri and Ansmann (2016) for a higher supersaturation of 0.4 %, the total maximum CCN number concentrations of each case were right in line with the average of 1060 ± 400 cm⁻³, that was found by Andreae (2009) for polluted marine regions.

Regarding INP number concentrations, dust provided more INP in the case of immersion freezing. In this freezing regime, an increase in n_{INP} of about two orders of magnitudes per 10 K was found, reflecting the findings of Mamouri and Ansmann (2016).

In contrast, the applied deposition freezing parameterisation favored soot-related INP, although the difference to $n_{\text{INP,d}}$ was smaller at the lowest tested temperature of -55 °C. However, since the number concentration of soot INP was calculated using continental aerosol surface area concentrations, the found numbers are to be interpreted as rough estimates, especially in cases of little soot contribution to the continental aerosol.

Furthermore, the vertical profiles of lidar-based derived particle number concentrations of particles with radius > 250 nm, $n_{250,\text{dry}}$, were compared to the preliminary results of A-LIFE's airborne in-situ measurements of particle number concentrations of particles with radius > 280 nm, n_{280} . While locally influenced and systematic differences could be identified in all three comparisons, an overall good agreement was achieved for the

lofted layers, which are brought to Cyprus via long-range transport and are thus of regional influence. This result further substantiates the applicability of the data analysis scheme given by Mamouri and Ansmann (2016) for the derivation of aerosol microphysical properties from lidar observations. Hence, the remote sensing instrument lidar also gains importance in the field of aerosol and cloud research.

While this work mainly aimed to provide detailed knowledge of the aerosol conditions encountered during April 2017 in Limassol, Cyprus, some of the presented results already serve as input for a data assimilation exercise for the desert dust forecast models in the frame of the ACTRIS-2 project.

Furthermore, as the analysis of the data sets accumulated during A-LIFE's field campaign is still in progress, a more comprehensive comparison of lidar and in-situ results will be possible in the future. The ongoing closure between the two may lead to a better understanding of cloud-formation-relevant particles and thus supplement model simulations of aerosol-cloud-interactions.

List of Figures

1.1	Sketch indicating the aerosol transport to Cyprus in the Eastern Mediterranean. (Picture provided by TROPOS)	2
2.1	Classification of different aerosol types by lidar and depolarisation ratio at 355 nm. The used data includes measurements by TROPOS (dots) and the University of Munich (open squares) at Cape Verde, Leipzig, Munich, the Amazon Basin and over the North Atlantic (Illingworth et al., 2015).	10
2.2	Overview of the data analysis scheme used to derive the microphysical particle properties, and the estimated cloud-relevant quantities from aerosol optical properties. The use of a polarisation lidar allows for the separation of dust and non-dust backscatter coefficients β_d and β_{nd} via the particle depolarisation ratio. The distinction of the non-dust contribution into marine (β_m) and continental aerosol backscatter coefficients (β_c) may then be made utilising backward trajectory analysis and Ångström exponent information. The three backscatter coefficients are converted to respective extinction coefficients α_i , which are then converted to particle number concentrations $n_{100,d,dry}$, $n_{50,m,dry}$, $n_{50,c,dry}$ and $n_{250,i,dry}$, and surface area concentrations $s_{i,dry}$. Indices indicate the minimum dry radius in nanometers and aerosol type. In the last step, estimates of CCN number concentrations $n_{CCN,i}$ are calculated from $n_{100,d,dry}$, $n_{50,m,dry}$, $n_{50,c,dry}$, while estimates of INP number concentrations $n_{INP,i}$ are derived from $s_{i,dry}$. Adapted from Mamouri and Ansmann (2016).	12
3.1	The measurement systems of LACROS, deployed in Limassol. (Picture provided by TROPOS)	20
3.2	Dates of Polly ^{XT} measurements during CyCARE (Leibniz Institute for Tropospheric Research, 2018b).	20
3.3	Total flight path (red) of DLR Falcon during April, 2017. (Picture provided by TROPOS)	23
4.1	Time-height plot of the range-corrected signal at 1064 nm, retrieved on 06 April 2017, 00:00-03:00 UTC at Limassol, Cyprus. The period of the automatic daily depolarisation calibration (indicated by the blue bar) was excluded from the calculation of averaged vertical profiles.	26

4.2	5-day NOAA HYSPLIT backward trajectories of airmasses at 500 (red), 2500 (blue), and 4500 m (green) altitude, arriving in Limassol, Cyprus, on 06 April 2017, 02:00 UTC (NOAA Air Resources Laboratory, 2018).	27
4.3	Averaged profiles of backscatter and extinction coefficient, lidar ratio, Ångström exponent and particle depolarisation ratio for the period of 06 April 2017, 00:00-03:00 UTC at Limassol, Cyprus. Backscatter coefficients and depolarisation ratios are vertically smoothed with 187.5 m; extinction coefficients, lidar ratios, and Ångström exponents with 742.5 m.	27
4.4	Vertical profiles of aerosol-type-dependent backscatter coefficients (left), mass concentrations (middle), and extinction coefficients (right). The total 532 nm particle backscatter coefficient profile of 06 April 2017, 00:00-03:00 UTC at Limassol, Cyprus, served as input after a vertical smoothing of 742.5 m had been applied. Used lidar ratios are 40 sr for dust, 30 sr for non-dust, 20 sr for marine, and 35 sr for continental aerosol.	28
4.5	Vertical profiles of the number concentrations of particles with dry radius > 50 nm, in the case of marine and continental aerosol, and > 100 nm, in the case of desert dust, (left panel), as well as of particles with dry radius > 250 nm (middle panel) and surface area concentrations (right panel), derived via Eq. 2.34-2.42 from the particle-type-dependent extinction coefficient profiles of 06 April 2017, 00:00-03:00 UTC.	29
4.6	Vertical profiles of estimated CCN number concentrations, following Eq. 2.43-2.45 at an assumed supersaturation of 0.25 % (left), as well as INP number concentrations, as derived using Ullrich et al. (2017)'s parameterisations for immersion freezing ($T=-20^{\circ}\text{C}$ and -30°C) and deposition freezing ($T=-45^{\circ}\text{C}$ and -55°C), for the period of 06 April 2017, 00:00-03:00 UTC. Relative uncertainties are typically in the range of factor 2-3 for n_{CCN} , and of factor 3-10 for n_{INP}	30
4.7	Time-height plot of the range-corrected signal at 1064 nm, retrieved on 06 April 2017, 04:30-08:05 UTC at Limassol, Cyprus. In order to exclude clouds, only the time period of 06:00-08:05 UTC was analysed.	32
4.8	Averaged profiles of backscatter and extinction coefficient, Ångström exponent and particle depolarisation ratio for the period of 06 April 2017, 06:00-08:05 UTC at Limassol, Cyprus. Lidar ratios of 39 sr for 355 nm and 44 sr for 532 nm were assumed. The vertical smoothing length for all profiles is 367.5 m.	32
4.9	Same as Fig. 4.4 but for 06 April 2017, 06:00-08:05 UTC. Used lidar ratios are 40 sr for dust, 50 sr for non-dust, 20 sr for marine, and 60 sr for continental aerosol.	33
4.10	Same as Fig. 4.5 but for 06 April 2017, 06:00-08:05 UTC.	34
4.11	Same as Fig. 4.6 but for 06 April 2017, 06:00-08:05 UTC.	35

4.12	Time-height plot of the range-corrected signal at 1064 nm, retrieved on 21 April 2017, 11:50-16:00 UTC at Limassol, Cyprus.	36
4.13	7-day NOAA HYSPLIT backward trajectories of airmasses at 500 (red), 4000 (blue), and 5500 m (green) altitude, arriving in Limassol, Cyprus, on 21 April 2017, 16:00 UTC (NOAA Air Resources Laboratory, 2018). . .	37
4.14	Averaged profiles of backscatter and extinction coefficient, Ångström exponent and particle depolarisation ratio for the period of 21 April 2017, 11:50-16:00 UTC at Limassol, Cyprus. Lidar ratios of 47 sr for 355 nm and 43 sr for 532 nm were assumed. The vertical smoothing length for all profiles is 367.5 m.	38
4.15	Same as Fig. 4.4 but for 21 April 2017, 11:50-16:00 UTC. Used lidar ratios are 45 sr for dust, 30 sr for non-dust, 20 sr for marine, and 35 sr for continental aerosol.	39
4.16	Same as Fig. 4.5 but for 21 April 2017, 11:50-16:00 UTC.	40
4.17	Same as Fig. 4.6 but for 21 April 2017, 11:50-16:00 UTC.	41
4.18	Time-height plot of the range-corrected signal at 1064 nm, retrieved on 21 April 2017, 17:00-20:00 UTC at Limassol, Cyprus.	42
4.19	Averaged profiles of backscatter and extinction coefficient, lidar ratio, Ångström exponent and particle depolarisation ratio for the period of 21 April 2017, 17:00-20:00 UTC at Limassol, Cyprus. Backscatter coefficients and depolarisation ratios are vertically smoothed with 187.5 m; extinction coefficients, lidar ratios, and Ångström exponents with 742.5 m.	43
4.20	Same as Fig. 4.4 but for 21 April 2017, 17:00-20:00 UTC. Used lidar ratios are 50 sr for dust, 40 sr for non-dust, 20 sr for marine, and 45 sr for continental aerosol.	44
4.21	Same as Fig. 4.5 but for 21 April 2017, 17:00-20:00 UTC.	44
4.22	Same as Fig. 4.6 but for 21 April 2017, 17:00-20:00 UTC.	45
4.23	Time-height plot of the range-corrected signal at 1064 nm, retrieved on 26 April 2017, 21:00-23:30 UTC at Limassol, Cyprus. The period of the automatic daily depolarisation calibration (indicated by the blue bar) was excluded from the calculation of averaged vertical profiles.	46
4.24	5-day NOAA HYSPLIT backward trajectories of airmasses at 500 (red), 2000 (blue), and 5000 m (green) altitude, arriving in Limassol, Cyprus, on 27 April 2017, 09:00 UTC (NOAA Air Resources Laboratory, 2018). . .	47
4.25	Averaged profiles of backscatter and extinction coefficient, lidar ratio, Ångström exponent and particle depolarisation ratio for the period of 26 April 2017, 21:00-23:30 UTC at Limassol, Cyprus. Backscatter coefficients and depolarisation ratios are vertically smoothed with 187.5 m; extinction coefficients, lidar ratios, and Ångström exponents with 742.5 m.	48

4.26	Same as Fig. 4.4 but for 26 April 2017, 21:00-23:30 UTC. Used lidar ratios are 35 sr for dust, 30 sr for non-dust, 20 sr for marine, and 35 sr for continental aerosol.	49
4.27	Same as Fig. 4.5 but for 26 April 2017, 21:00-23:30 UTC.	50
4.28	Same as Fig. 4.6 but for 26 April 2017, 21:00-23:30 UTC.	51
4.29	Time-height plot of the range-corrected signal at 1064 nm, retrieved on 27 April 2017, 07:15-10:15 UTC at Limassol, Cyprus.	52
4.30	Averaged profiles of backscatter and extinction coefficient, Ångström exponent and particle depolarisation ratio for the period of 27 April 2017, 07:15-10:15 UTC at Limassol, Cyprus. Lidar ratios of 42 sr for 355 nm and 38 sr for 532 nm were assumed. The vertical smoothing length for all profiles is 367.5 m.	53
4.31	Same as Fig. 4.4 but for 27 April 2017, 07:15-10:15 UTC. Used lidar ratios are 38 sr for dust, 30 sr for non-dust, 20 sr for marine, and 35 sr for continental aerosol.	54
4.32	Same as Fig. 4.5 but for 27 April 2017, 07:15-10:15 UTC.	54
4.33	Same as Fig. 4.6 but for 27 April 2017, 07:15-10:15 UTC.	55
5.1	Overview of DLR Falcon’s flight tracks on 06 April 2017, 04:30-08:05 UTC; 21 April 2017, 11:48-16:01 UTC; and 27 April 2017, 07:13-10:18 UTC.	58
5.2	Comparison of the sum of the lidar-derived $n_{250,i}$, shown in chapter 4, with preliminary in-situ CAS measurements, provided by A-LIFE’s PI, Bernadett Weinzierl, for each of the three daytime measurement periods.	58

List of Tables

2.1	Applied values for each of the parameters required for the determination of dust and non-dust contributions and the subsequent calculation of extinction coefficient and mass concentration profiles. Depolarisation ratios δ_i , particle densities ρ_i and conversion factors ν_i/τ_i are taken from literature. Lidar ratios S_i at 532 nm were varied within the range of literature values in order to find the best match between the calculated and measured extinction coefficients for each case discussed in chapter 4. . . .	14
2.2	Conversion parameters used for the calculation of particle number and surface area concentration profiles. Adapted from Mamouri and Ansmann (2016).	16
2.3	Typical uncertainty ranges of the various aerosol properties. Adapted from Mamouri and Ansmann (2016).	18
3.1	List of instruments aboard the DLR Falcon for A-LIFE. Dp indicates the particle diameter (University of Vienna, 2018b).	22
3.2	Overview of DLR Falcon flights performed during April 2017. The airport location is indicated in paranthesis: DE corresponds to Oberpfaffenhofen, Germany, IT to Cagliari, Italy, CY to Paphos, Cyprus, GR to Heraklion, Greece, and MT to Malta. Adapted from University of Vienna (2018a). .	24
4.1	Overview of the maximum values of mass concentration in $\mu\text{g m}^{-3}$, CCN number concentration n_{CCN} in cm^{-3} , and INP number concentration n_{INP} at -30°C in L^{-1} as they were derived from the lidar observation of each time period.	56

Bibliography

- Albrecht, B. A. (1989). Aerosols, Cloud Microphysics, and Fractional Cloudiness. *Science*, 245(4923):1227–1230.
- Andreae, M. O. (2009). Correlation between cloud condensation nuclei concentration and aerosol optical thickness in remote and polluted regions. *Atmos. Chem. Phys.*
- Ansmann, A., Riebesell, M., and Weitkamp, C. (1990). Measurement of atmospheric aerosol extinction profiles with a Raman lidar. *Optics letters*, 15(13):746–748.
- Ansmann, A., Seifert, P., Tesche, M., and U.Wandinger (2012). Profiling of fine and coarse particle mass: Case studies of Saharan dust and Eyjafjallajökull/Grimsvötn volcanic plumes. *Atmos. Chem. and Phys.*
- Ansmann, A., Tesche, M., Seifert, P., Groß, S., Freudenthaler, V., Apituley, A., Wilson, K. M., Serikov, I., Linné, H., Heinold, B., Hiebsch, A., Schnell, F., Schmidt, J., Mattis, I., Wandinger, U., and Wiegner, M. (2011). Ash and fine-mode particle mass profiles from EARLINET-AERONET observations over central Europe after the eruptions of the Eyjafjallajökull volcano in 2010. *Journal of Geophysical Research: Atmospheres*.
- Ansmann, A., Wandinger, U., Riebesell, M., Weitkamp, C., and Michaelis, W. (1992). Independent measurement of extinction and backscatter profiles in cirrus clouds by using a combined Raman elastic-backscatter lidar. *Applied Optics*, 31:7113–7131.
- Baars, H., Ansmann, A., Althausen, D., Engelmann, R., Heese, B., Müller, D., Artaxo, P., Paixao, M., Pauliquevis, T., and Souza, R. (2012). Aerosol profiling with lidar in the Amazon Basin during the wet and dry season. *Journal of Geophysical Research: Atmospheres*, 117(D21).
- Baars, H., Kanitz, T., Engelmann, R., Althausen, D., Heese, B., Komppula, M., Preißler, J., Tesche, M., Ansmann, A., Wandinger, U., et al. (2016). An overview of the first decade of Polly NET: an emerging network of automated Raman-polarization lidars for continuous aerosol profiling. *Atmospheric Chemistry and Physics*, 16(8):5111–5137.
- Department of Meteorology, Republic of Cyprus (2018). Climate of Cyprus. http://www.moa.gov.cy/moa/ms/ms.nsf/DMLcyclimate_en/DMLcyclimate_en?OpenDocument. Accessed January 5, 2018.

- Emersic, C. (2018). Cloud Physics Research - Formation of Ice Crystals. <http://www.cas.manchester.ac.uk/resactivities/cloudphysics/topics/formation/>. Accessed January 5, 2018.
- Engelmann, R., Kanitz, T., Baars, H., Heese, B., Althausen, D., Skupin, A., Wandinger, U., Komppula, M., Stachlewska, I. S., Amiridis, V., et al. (2016). The automated multiwavelength Raman polarization and water-vapor lidar Polly XT: the neXT generation. *Atmospheric Measurement Techniques*, 9(4):1767–1784.
- Freudenthaler, V., Esselborn, M., Wiegner, M., Heese, B., Tesche, M., Ansmann, A., MüLLER, D., Althausen, D., Wirth, M., Fix, A., Ehret, G., Knippertz, P., Toledano, C., Gasteiger, J., Garhammer, M., and Seefeldner, M. (2009). Depolarization ratio profiling at several wavelengths in pure Saharan dust during SAMUM 2006. *Tellus B: Chemical and Physical Meteorology*, 61(1):165–179.
- Groß, S., Freudenthaler, V., Wiegner, M., Gasteiger, J., Geiß, A., and Schnell, F. (2012). Dual-wavelength linear depolarization ratio of volcanic aerosols: Lidar measurements of the Eyjafjallajökull plume over Maisach, Germany. *Atmospheric Environment*, 48:85–96.
- Groß, S., Tesche, M., Freudenthaler, V., Toledano, C., Wiegner, M., Ansmann, A., Althausen, D., and Seefeldner, M. (2011). Characterization of Saharan dust, marine aerosols and mixtures of biomass-burning aerosols and dust by means of multi-wavelength depolarization and Raman lidar measurements during SAMUM 2. *Tellus B*, 63(4):706–724.
- Illingworth, A. J., Barker, H. W., Beljaars, A., Ceccaldi, M., Chepfer, H., Clerbaux, N., Cole, J., Delanoë, J., Domenech, C., Donovan, D. P., Fukuda, S., Hiraakata, M., Hogan, R. J., Huenerbein, A., Kollias, P., Kubota, T., Nakajima, T., Nakajima, T. Y., Nishizawa, T., Ohno, Y., Okamoto, H., Oki, R., Sato, K., Satoh, M., Shephard, M. W., Velázquez-Blázquez, A., Wandinger, U., Wehr, T., and van Zadelhoff, G.-J. (2015). The EarthCARE Satellite: The Next Step Forward in Global Measurements of Clouds, Aerosols, Precipitation, and Radiation. *Bulletin of the American Meteorological Society*, 96(8):1311–1332.
- IPCC (2013). Climate Change 2013: The Physical Science Basis. *Cambridge University Press*, page 1535 pp.
- Kanitz, T., Ansmann, A., Engelmann, R., and Althausen, D. (2013). North-south cross sections of the vertical aerosol distribution over the Atlantic Ocean from multiwavelength Raman/polarization lidar during Polarstern cruises. *Journal of Geophysical Research: Atmospheres*, 118(6):2643–2655.

- Klett, J. (1981). Stable analytical inversion solution for processing lidar returns. *Applied Optics*, 20:211–220.
- Koehler, K. A., Kreidenweis, S. M., DeMott, P. J., Petters, M.-D., Prenni, A. J., and Carrico, C. M. (2009). Hygroscopicity and cloud droplet activation of mineral dust aerosol. *Geophys. Res. Lett.*, 36(8).
- Kumar, P., Sokolik, I. N., and Nenes, A. (2011). Measurements of cloud condensation nuclei activity and droplet activation kinetics of fresh unprocessed regional dust samples and minerals. *Atmospheric Chemistry and Physics*, 11(7):3527–3541.
- Leibniz Institute for Tropospheric Research (2018a). Cyprus Clouds Aerosols and Rain Experiment (CyCARE). <https://www.tropos.de/institut/abteilungen/fernerkundung-atmosphaerischer-prozesse-neu/ag-bodengebundene-fernerkundung/cyprus-clouds-aerosols-and-rain-experiment-cycare/>. Accessed January 5, 2018.
- Leibniz Institute for Tropospheric Research (2018b). TROPOS PollyXT-Quicklooks. http://lacros.rsd.tropos.de/cloudnet/public.html/realtime/archive/limassol_pollyxt/index.html. Accessed March 4, 2018.
- Mamouri, R. E. and Ansmann, A. (2014). Fine and coarse dust separation with polarization lidar. *Atmospheric Measurement Techniques*, 7(11):3717–3735.
- Mamouri, R.-E. and Ansmann, A. (2016). Potential of polarization lidar to provide profiles of CCN-and INP-relevant aerosol parameters. *Atmospheric Chemistry and Physics*, 16(9):5905–5931.
- Mamouri, R.-E. and Ansmann, A. (2017). Potential of polarization/Raman lidar to separate fine dust, coarse dust, maritime, and anthropogenic aerosol profiles. *Atmospheric Measurement Techniques*, 10(9):3403–3427.
- NASA Goddard Space Flight Center (2018). AERONET Data Display - Site: CUT-TEPAK. https://aeronet.gsfc.nasa.gov/cgi-bin/type_one_station_opera_v2_new?site=CUT-TEPAK&nachal=0&year=25&month=3&aero_water=0&level=1&if_day=0&if_err=0&place_code=10&year_or_month=0. Accessed May 10, 2018.
- Nisantzi, A., Mamouri, R. E., Ansmann, A., Schuster, G. L., and Hadjimitsis, D. G. (2015). Middle East versus Saharan dust extinction-to-backscatter ratios. *Atmospheric Chemistry and Physics*, 15(12):7071–7084.
- NOAA Air Resources Laboratory (2018). HYSPLIT Trajectory Model. <https://ready.arl.noaa.gov/HYSPLIT.php>. Accessed January 5, 2018.

- Tesche, M., Ansmann, A., Müller, D., Althausen, D., Engelmann, R., Freudenthaler, V., and Groß, S. (2009a). Vertically resolved separation of dust and smoke over Cape Verde using multiwavelength Raman and polarization lidars during Saharan Mineral Dust Experiment 2008. *Journal of Geophysical Research: Atmospheres*, 114(D13). D13202.
- Tesche, M., Ansmann, A., Müller, D., Althausen, D., Mattis, I., Heese, B., Freudenthaler, V., Wiegner, M., Esselborn, M., Pisani, G., and Knippertz, P. (2009b). Vertical profiling of Saharan dust with Raman lidars and airborne HSRL in southern Morocco during SAMUM. *Tellus B*, 61(1):144–164.
- Tesche, M., Gross, S., Ansmann, A., Müller, D., Althausen, D., Freudenthaler, V., and Esselborn, M. (2011). Profiling of Saharan dust and biomass-burning smoke with multiwavelength polarization Raman lidar at Cape Verde. *Tellus B*, 63(4):649–676.
- Tobo, Y. (2016). An improved approach for measuring immersion freezing in large droplets over a wide temperature range. *Scientific reports*, 6:32930.
- Twomey, S. (2007). Pollution and the Planetary Albedo. *Atmospheric Environment*, 41:120 – 125.
- Ullrich, R., Hoose, C., Möhler, O., Niemand, M., Wagner, R., Höhler, K., Hiranuma, N., Saathoff, H., and Leisner, T. (2017). A New Ice Nucleation Active Site Parameterization for Desert Dust and Soot. *Journal of the Atmospheric Sciences*, 74(3):699–717.
- University of Vienna (2018a). A-LIFE Flight Overview. <https://a-life.at/flight-overview/>. Accessed July 6, 2018.
- University of Vienna (2018b). A-LIFE Instrumentation. <https://www.a-life.at/instrumentation/>. Accessed January 6, 2018.
- University of Vienna (2018c). A-LIFE Project Description. <https://www.a-life.at/project-description/>. Accessed January 6, 2018.
- Veselovskii, I., Goloub, P., Podvin, T., Bovchaliuk, V., Derimian, Y., Augustin, P., Fourmentin, M., Tanre, D., Korenskiy, M., Whiteman, D. N., Diallo, A., Ndiaye, T., Kolgotin, A., and Dubovik, O. (2016). Retrieval of optical and physical properties of African dust from multiwavelength Raman lidar measurements during the SHADOW campaign in Senegal. *Atmospheric Chemistry and Physics*, 16(11):7013–7028.
- Wandinger, U. (2005). *Lidar - Range resolved optical remote sensing of the atmosphere*. Springer Science.
- Weinzierl, B. (2014). ERC Starting Grant - Research Proposal for A-LIFE (Absorbing aerosol layers in a changing climate: aging, lifetime, and dynamics).

Statement of Authenticity

I hereby certify that this master thesis has been composed by myself and contains no copy or paraphrase of material previously published or written by another person unless otherwise acknowledged in the text. All references and verbatim extracts have been quoted, and all sources of information have been specifically acknowledged. It has not been accepted in any previous application for the award of any other degree in any tertiary institution.

Leipzig, 23 October 2018

.....
Claudia Urbanneck